J. Fluid Mech. (2009), *vol.* 641, *pp.* 85–113. © Cambridge University Press 2009
doi:10.1017/S0022112009991431

Spatio-temporal mode dynamics and higher order transitions in high aspect ratio Newtonian Taylor–Couette flows

CARI S. DUTCHER AND SUSAN J. MULLER†
Department of Chemical Engineering, University of California at Berkeley, Berkeley, CA 94720, USA

(Received 19 December 2008; revised 29 July 2009; accepted 30 July 2009; first published online 17 November 2009)

Spatial and temporal frequency dynamics were experimentally tracked via flow visualization for Newtonian fluids as a function of the inner cylinder Reynolds number (Re_i) in the flow between concentric, independently rotating cylinders with a radius ratio of 0.912 and an aspect ratio of 60.7. Eight transitions from laminar to turbulent flow were characterized in detail for a stationary outer cylinder, producing highly resolved space–time and frequency–time plots for wavy, modulated and weakly turbulent states. A previously unreported early-modulated wavy vortex flow was found in our high aspect ratio geometry both with and without the presence of a dislocation. The envelope of stability for this flow state was shown to cross into the co-rotating regime, and is present up to $Re_o \sim 60$, where Re_o is the outer cylinder Reynolds number. This early modulation is independent of acceleration in the range $0.18 < \mathrm{d}Re_i/\mathrm{d}\tau < 2.9$, where τ is the time nondimensionalized with a viscous time scale. While many of the flow states have been previously observed in geometries with somewhat different radius ratios, we provide new characterization of transitional structures for $Re_o = 0$ in the range $0 < Re^* < 21.4$, where $Re^* = Re_i/Re_c$ and Re_c is the value of Re_i at the primary instability. Special attention has been given to ramp rate. For quasi-static ramps, axisymmetric states are stable over the ranges of $Re^* = [(0\text{–}1.17), > 15.4]$, states characterized by a single distinct temporal frequency for $Re^* = [(1.17\text{–}1.41), (3.56\text{–}5.20), (7.85\text{–}15.4)]$, states with multiple temporal frequencies for $Re^* = [(1.41\text{–}3.56), (5.20\text{–}7.85)]$, and a transition from laminar to weakly turbulent vortices occurs at $Re^* = 5.49$. All flow states are characterized by symmetry/symmetry-breaking features as well as azimuthal and axial wavenumbers.

Key words: instability, Taylor–Couette flow, transition to turbulence

1. Introduction

Taylor–Couette (T-C) flow, or flow between two concentric, rotating cylinders, has long been an interesting and challenging problem due to its rich nonlinear dynamics. As the angular velocities of the inner and outer cylinders are varied, many flow states, separating unidirectional shear flow and fully developed turbulent flow, can be accessed. Consequently, significant insight into flow properties and dynamics has been gained from this unique geometry. The T-C geometry is parameterized by a radius ratio $\eta = R_i/R_o$, where R_i and R_o are the radii of the inner and outer cylinders, respectively, and an aspect ratio $\Gamma = h/d$, where h is the cylinder height and d is the

---

† Email address for correspondence: muller2@berkeley.edu

gap, $d = R_o - R_i$. In the present study, $\eta = 0.912$ and $\Gamma = 60.7$. Reynolds numbers Re_i and Re_o based on the radii and the angular velocities Ω_i and Ω_o of the inner and outer cylinders, respectively, are defined here as $Re_i = \Omega_i d R_i/\nu$ and $Re_o = \Omega_o d R_o/\nu$, where ν is the kinematic viscosity. The primary transition from Couette flow occurs at Re_c, the critical Reynolds number based on Re_i, and depends on η and Re_o. For the present work, $Re_c(\eta = 0.912,\ Re_o = 0) = 140.2$, as given by linear stability theory. Higher order critical conditions are cast in terms of $Re^* = Re_i/Re_c(\eta,\ Re_o)$.

For experiments where $Re_o = 0$, flow states found when increasing Re_i, include Taylor vortex flow (TVF), wavy vortex flow (WVF) and modulated wavy vortex flow (MWV). TVF is a flow pattern of time-independent, axisymmetric, toroidal vortices characterized by a single axial wavenumber. WVF consists of time-dependent, non-axisymmetric vortices characterized by a single axial wavenumber and a single azimuthal wavenumber. MWV, characterized in detail by Gorman and Swinney (1982), involves non-axisymmetric vortices described by two temporal frequencies. As Re_i is further increased, a 'chaotic' transition occurs at the onset of non-periodic small-scale spatial structure and a smoothly decaying spectral profile, while the large scale, axially periodic structure remains (see e.g. Brandstater and Swinney 1987). Flow states after this transition are sometimes referred to as 'post-chaotic' or 'weakly turbulent' flows. Based on spectral analysis, these weakly turbulent states, defined in terms of their coherent structure, are subdivided into three flow states. The first is chaotic wavy vortex flow (CWV; the notation of CWV is from Takeda 1999, and is applied less broadly here), which contains multiple dominant temporal frequencies. The second and third post-chaotic flows are wavy turbulent vortex flow (WTV) and turbulent Taylor vortex flow (TTV) with coherent structures that are characterized by one and zero distinct temporal frequencies, respectively. Subsequent transitions are not explored in this paper.

Over the past 85 years there has been extensive experimental work on the Newtonian Taylor–Couette problem (including seminal work by Taylor 1923, Coles 1965 and Andereck, Liu & Swinney 1986; recent reviews include those by Koschmieder 1993, Tagg 1994 and Abshagen, Schulz and Pfister 1996). Collectively, the experimental studies have covered a large parameter space, including varying radius ratio η, aspect ratio Γ, rotation ratio $\Omega_o/\Omega_i = \eta Re_o/Re_i$ and ramp rate $\mathrm{d}Re_i/\mathrm{d}\tau$, where τ is time made dimensionless with the viscous time scale d^2/ν. However, due to the vastness of the parameter space, a complete set of parameter permutations has not yet been realized and much of the parameter space remains undercharacterized. In this paper, we offer detailed experimental results for our geometry of lower- and higher-order transitions to fill in some of the gaps in the $Re_o = 0$ and $Re_o > 0$ regimes. Here, we briefly discuss the effects of varying η and Γ as reported in the literature, focusing on $Re_o = 0$ except where noted. The discussion on the effects of Re_o and $\mathrm{d}Re_i/\mathrm{d}\tau$ is postponed until the end of this introduction and § 2.2, respectively.

Radius ratio dictates the relative range of streamline curvature experienced by the fluid. The non-monotonic effect of η on the first transition (TVF) has long been understood and approximate expressions for $Re_c(\eta)$ are available (cf. Esser & Grossmann 1996; Dutcher & Muller 2007). The effect of η on the second-order transition (WVF), a Hopf bifurcation, is also known: DiPrima, Eagles & Ng (1984) compiled experimental data for $Re_{c\_WVF}(\eta,\ Re_o = 0)$ and showed that as $\eta \to 1$, WVF was stabilized (whereas TVF is destabilized). However, as Re_i increases, even with $Re_o = 0$, critical conditions and characterization data for post-WVF flow states are extremely limited (e.g. von Stamm *et al.* 1996; Meincke and Egbers 1999), and generalizations on the effect of η on these higher order transitions are not readily available.

A major difficulty in establishing a generic sequence of transitions to turbulence for ‘narrow’ or ‘wide’ gap geometries is the sensitivity of higher order transitions to aspect ratio. Walden and Donnelly (1979), with $Re_o = 0$, $\eta = 0.876$ and $18 < \Gamma < 80$, showed that the critical conditions for the transitions to turbulence are dependent on aspect ratio. Cole (1976) examined WVF critical conditions as a function of Γ and found that for short cylinders ($\Gamma < 20$), the end walls suppress the formation of WVF, due to the Ekman layers (Czarny *et al.* 2004). Mullin (1985) also reported a significant change, especially for wide gap systems, in both the critical condition for WVF and the azimuthal mode number as Γ was varied from 13 to 32.

While end effects notably impact geometries with small aspect ratios, geometries with large aspect ratios are indelibly marked by mode or flow type competition. As noted by Abshagen, Pfister and Mullin (2001) regarding the comprehensive set of experiments preformed for $\eta = 0.5$ (von Stamm *et al.* 1996; Abshagen *et al.* 2001, 2005), the rationale behind the choice of a small aspect ratio of $\Gamma \sim 3$–4 was to limit the degree of mode competition. Benjamin and Mullin (1982) indicate that for large aspect ratios, the ‘high multiplicity’ of solutions is significant. They found that even for $\Gamma = 12.6$, fifteen different flows could be produced under identical conditions of $\eta = 0.6$, $Re_i = 359$ and $Re_o = 0$. In Coles’ (1965) seminal work, with $\eta = 0.874$, $\Gamma = 27.9$ and $Re_o = 0$, more than 20 WVF states could be reached at a given Re_i, depending on ‘the whole previous history of the experiment’. This multiplicity of flow states may also help to explain the difficultly in establishing a general pathway of transitions in T-C flows.

In high aspect ratio geometries similar to the one we explore, other authors have occasionally noted the effect of this multiplicity in the form of alternating WVF states separated by mixed-mode states (defined by the appearance of broad spectral peaks). This transitional non-WVF state separating WVF states is believed to be first found by Donnelly *et al.* (1980), who studied WVF transitions with $\eta = 0.876$ and $\Gamma = 80$. With $\eta \cong 0.88$, both Park and Crawford (1983) and Ahlers, Cannell & Dominguez-Lerma (1983) also reported seeing dislocations (‘turbutors’; cf. Donnelly and LaMar 1988) preceding WVF transitions, complete with broadened spectral peaks. King and Swinney (1983) also found these regions of transition separating wavy modes for high aspect ratios (>32), preventing them from identifying the stability of a certain wave state due to the ‘extensive distortions that persist in the flow pattern near some parts of the stability boundary’. While this multiplicity of flow states is clear in the WVF regime, the question is ‘are these transitional mixed-mode states stable?’ Beyond the literature reviewed above, this interesting mixed-mode phenomena and regime has yet to receive detailed dynamic characterization as a function of Re_i and the question of its stability remains unresolved.

As Re_i is increased beyond WVF and these transitional flows, MWV is commonly observed. Gorman and Swinney (1982) found 12 distinct modulated wave states, produced through a variety of initial conditions, with $\eta = 0.88$ and $\Gamma = 20$. At still higher Re_i, a chaotic flow emerges, chaotic wavy vortex flow (CWV), and overlaps with the MWV, followed by WTV and turbulent Taylor vortex flow (TTV) (e.g. Barcilon *et al.* 1979; Fenstermacher, Swinney & Gollub 1979; Koschmieder 1979; Walden & Donnelly 1979; Takeda 1999). Featureless turbulence (Smith & Townsend 1982; Lathrop, Fineberg, & Swinney 1992) and ensuing flow states involving the re-emergence of a fast azimuthal wave seen by Takeda (1999), Wang, Olsen & Vigil (2005) and Walden and Donnelly (1979) are not explored in this paper.

These post-WVF states have been well documented in the literature for a geometry of $\eta \cong 0.88$ and $\Gamma \cong 20$ (see e.g. Gollub and Swinney 1975; Fenstermacher *et al.* 1979; Gorman and Swinney 1982; Brandstater and Swinney 1987). In general, the reported pathway consists of transitions to MWV in the range of $Re^* = 9$–10, chaotic flow around $Re^* = 11$–12, loss of a modulated temporal frequency around $Re^* = 18$–19 and TTV near $Re^* = 21$. Similar transitions were also found with $\eta = 0.904$, $\Gamma = 20$, in a series of papers by Takeda (1999) and Takeda *et al.* (1992, 1993). Barcilon *et al.* (1979), with $\eta = 0.908$ and $\Gamma = 65$, describe a slightly different transition to TTV. However, while Barcilon *et al.* (1979) do not rigorously define their ramping protocol, comments about how the use of air instead of a high viscosity oil yielded differences in the value and number of predominant wavenumbers suggest that a constant dimensionless ramp rate was not used.

When the constraint that the outer cylinder is stationary (i.e. $Re_o = 0$) is relaxed, the value of Re_o plays an important role on Re_c (Taylor 1923; Donnelly & Fultz 1960; Coles 1965; Snyder 1968; Andereck *et al.* 1986) as well as on higher order instabilities. A very different behaviour is observed in the co- and counter-rotational regimes, corresponding to $Re_o > 0$ and $Re_o < 0$, respectively. Andereck *et al.* (1986), in their seminal paper, mapped the stability boundaries for large portions of both the co- and the counter-rotational $Re_i - Re_o$ plane primarily for $\eta = 0.88$ and $\Gamma = 30$. In addition, Andereck, Dickman & Swinney (1983), Baxter & Andereck (1986) and Hegseth, Baxter & Andereck (1996) thoroughly mapped the co-rotational phase space, up to $Re_i \sim 2000$, and clearly defined flow states such as wavy inflow boundaries, wavy outflow boundaries, twisted vortices, and wavelets, again at $\eta = 0.88$, and $\Gamma = 30$. However, the co-rotational regime has not received detailed spectral analysis of the dynamic transitions between modes, early-modulated wavy states have not been reported and mappings have not been made for T-C geometries with aspect ratios > 30 or $\eta \neq 0.88$. While expressions for $Re_c(\eta, Re_o)$ exist for the primary instability (Coles 1967; Esser & Grossmann 1996; Dutcher & Muller 2007), there is no such description for secondary and higher flow states with a rotating outer cylinder, in large part due to the scarcity of experimental data available.

In this introduction, many experimental studies and their location in the multi-dimensional parameter space have been reviewed to emphasize the gaps in understanding of the Newtonian T-C problem, especially for higher order transitions to turbulence. Table 1 summarizes the geometries, Re_i range, Re_o range and the ramping protocol (when available) of some of the works cited above and a number of other relevant studies. The studies listed are representative of experiments in the $Re_o = 0$ and $Re_o > 0$ regimes that have accessed higher order flow states, demonstrating the wide range of η, Γ, $\mathrm{d}Re_i/\mathrm{d}\tau$, Re_o and Re_i used. As described above, an understanding of flows with mixed-mode features, weakly turbulent dynamics and $Re_o > 0$ would benefit from an increased library of characterization of flow regimes and transitions. Researchers interested in studies of tertiary variables (e.g. fluid elasticity, eccentricity of the cylinders and presence of a magnetic field) on a range of flow types will also benefit from the increased library of characterization offered here.

In this study, we examine flow transitions for a Taylor–Couette cell of radius ratio $\eta = 0.912$ and aspect ratio $\Gamma = 60.7$ in the range of $0 < Re^* < 21.4$. We focus primarily on flows with $Re_o = 0$, but we also consider co-rotational flows for $Re_o \leqslant 75$ and Re_i up to 550. We present the detailed temporal and spatial frequency evolution from Couette flow to TTV for multiple ramping conditions, using a quantitative methodology that has not been previously applied to pre-chaotic transitions or for co-rotational flows. The manner in which the Re_o, Re_i condition is reached (i.e. ramping protocol) plays an important role in the flow states accessed and the critical condition observed, and is given particular attention in our study. A review of previous

Authors	η	Γ	Re_o	Re_i/Re_c Range	Ramp protocol[h]
Abshagen *et al.* (2005)	0.5	3–3.25	0	∼4 to ∼12	*n/g*
Meincke & Egbers (1999)	0.5, 0.85	3.97, 13.2	0	1 to ∼27	“quasi-stationary”
Benjamin & Mullin (1982)	0.600	12.61	0	$Re_i = 359$	varied
Smith & Townsend (1982)	0.667	23.7	0	100 to ∼1500	*n/g*
Park *et al.* (1981)	0.678, 0.88	10.1–46.7	0	1	tested
Lathrop *et al.* (1992)	0.7246	11.47	0	$O(10^{\circ})$–$O(10^4)$	prepared state
Lewis & Swinney (1999)	0.724	11.4, 9.8	0	$O(10^1)$–$O(10^4)$	“slowly”
Koschmieder (1979)	0.727, 0.896	50, 123	0	1–200	tested
Wang *et al.* (2005)	0.733	34	0	6–200	prepared state[i]
Mullin (1985)	0.8, 0.83, 0.9	13–32	0	1–7.2	prepared state
King & Swinney (1983)	0.868	32–290[b]	0	1.4–8	$a < 0.47$
Coles (1965)	0.874, 0.881[a]	27.9	$(-8\text{ to }1)^{*}10^4$	1 to ∼170	varied
Brandstater & Swinney (1987)	0.875	20	0	∼10 to 26.3	*n/g*
Donnelly *et al.* (1980)	0.876	80	0	1–25	*n/g*
Walden & Donnelly (1979)	0.876	18–80	0	1–67[f]	“slowly”
Coughlin *et al.* (1991)	0.876	40	0	8.5–10	prepared state
Fenstermacher *et al.* (1979)	0.877	20	0	5.4–45	17/4 prepared
Gollub & Swinney (1975)	0.8756	19.8	0	1–22.75	“reversibly”
Park & Crawford (1983)	0.88	53.9, 62.16, 70.4	0	1^+ to 1.55	$a = 0.0089$[j]
Hegseth *et al.* (1996)	0.882	30	0–1100	1 to ∼17	$a < 0.667$
Xiao *et al.* (2002)	0.894	94	0	1–36	tested
Andereck *et al.* (1983)	0.883	30	500–1100	1 to ∼11	prepared state
Andereck *et al.* (1986)	0.883	20–48[c]	$(-4\text{ to }4)^{*}10^{3}$[e]	1–20+	$a = 0.79 \pm 0.086$[k]
Gorman & Swinney (1982)	0.883	20	0	6–25	varied
Zhang & Swinney (1985)	0.883	10–50[d]	0	1^+ to 10	*n/g*
Baxter & Andereck (1986)	0.883	30, 70	0–1000	1 to ∼17	$a < 0.667$
Ahlers *et al.* (1983)	0.893	53.9	0	1.2–1.6	“very slowly”
Takeda (1999)	0.904	20	0	7.1–145.6	ramped down[l]
Barcilon *et al.* (1979)	0.908	65	0	1 to ∼300[g]	“slowly”
Dutcher & Muller (2009)	0.912	60.7	−27 to 75	1–95	$a < 0.68$[m]

TABLE 1. Summary of the geometries, Re_o range, $Re^* = Re_i/Re_c(\eta)$ range and ramping protocol (when available) of many of the works cited in this paper.

---

[a] $\eta = 0.881$ precision cylinder used for multi-state problem, $\eta = 0.874$ rough cylinder used for $Re_o \neq 0$ work.

[b] Data only for $\Gamma = 32$.

[c] Primarily with $\Gamma = 30$.

[d] Primarily with $\Gamma = 20$.

[e] Transition data for $-4000 < Re_o < 1200$.

[f] Avoids region of $3 < Re^* < 15$.

[g] *R*esults obtained with different fluids. The region of $1 < Re^* < 4.47$ found using a high viscosity oil.

[h] Ramp Protocol: value for ‘*a*’ ($a = \mathrm{d}Re_i/\mathrm{d}\tau$) is listed either when the reference explicitly gives an ‘*a*’ value or when enough information is given about the ramp, geometric and fluid conditions to calculate a value. In all other cases, the protocol is listed as:
n/g = ramp protocol not given
tested = when the ramp rate is systematically varied as an independent variable
varied = varied ramps were used to access a variety of states
Descriptive words used in the paper, such as “slowly” or “reversibly”
prepared state = when a specific state is formed first (e.g. setting the axial and azimuthal wavenumber of WVF) and then Re_i was either held steady or ramped slowly from that state through other states, but the specific ramp rate is not given.
Exceptions to these cases are noted here:

[i] Ramped to $Re^* = 55$ with ‘*a*’ ∼8200, then either ramped up at the same rate or ramped down at ‘*a*’ ∼ 3300.

[j] Rate after TVF formation.

[k] Calculated assuming temperature in the range of 20–25°C.

[l] Primarily started at highest Re^* and ramped down with ‘small steps’.

[m] Modified ramp for $Re^* > 10.7$.

ramping protocols and a discussion of the ones used in this work are presented in § 2.2. For our geometry, we find a novel stabilization of an early MWV flow and assess its stability dependence on ramp rate as well as fully characterize its temporal and spatial frequency signature over the entire Re_i range. We also offer a unique characterization of some turbulent states and their structures and transitions. In addition, we propose a generic set of transitions to turbulence for our high aspect ratio, narrow gap geometry that agrees with experiments (for different η and Γ) summarized here, in which the local predominant temporal frequency increases and distinct temporal and spatial frequencies emerge and later decay with increasing Re_i.

2. Experimental procedure

2.1. *Taylor–Couette geometry*

The flow between concentric cylinders is accomplished using a custom-designed and built T-C cell for flow visualization and spectral analysis. The rotation of each cylinder is controlled independently. Temperature control, $\pm 0.1^\circ$C, is obtained via a continuously stirred paraffin oil bath in a Plexiglass box surrounding the outer cylinder. The oil surrounding the outer cylinder also reduces visual distortions by matching the refractive index of the curved glass outer cylinder. Stagnant mineral oil within the inner cylinder adds thermal mass to the system and helps stabilize the temperature. The size of the T-C cell, $R_i = 0.06946$ m, $R_o = 0.07615$ m and $h = 0.406$ m, makes it ideal for high resolution flow visualization and corresponds to a radius ratio $\eta = 0.912$ and an aspect ratio $\Gamma = 60.7$.

The flow visualization is realized using two CCD cameras that allow visualization of the (r, z) and (z, projected-Θ) planes and, through subsequent processing, space–time plots of the (z,t) and (r,t) planes. Quantitative information about the flow field can be obtained from these space–time plots (e.g. Abcha *et al.* 2008). In the present work, the visualization is achieved by seeding the solutions with anisotropic tracers (mica flakes); the orientation of the flakes by the flow field results in variations of the intensity of the light reflected from ambient lighting for the (z, projected-Θ) plane. For visualization in the (r, z) plane, an argon ion laser is directed through a Powell lens to create a thin light sheet oriented parallel to and containing the cylinder axis. Typical seeding levels of the mica flakes are 2×10^{-5} volume fraction. Captured images are then processed via background subtraction, normalization and spatial and temporal averaging techniques described elsewhere (White 2002). The control of image capture, processing and cylinder motion have been integrated in order to track rapidly evolving flows. Flow visualization and motion control is accomplished using a code developed on a LabVIEW platform, with the Compumotor motion control toolbox and the National Instruments vision development module. The image acquisition driver software is NI-IMAQ, which communicates with the IMAQ PCI-1409 frame grabber.

2.2. *Ramp rate*

The determination of the critical condition of an instability may depend strongly on the path used to access the state. For example, an instantaneous ramp to one parametric set of conditions may result in a different flow state than when those conditions are reached under "adiabatic" ramps. Due to this difference, a critically slow dimensionless ramp rate was determined and used for all fluids. The dimensionless ramp rate is an acceleration defined by the change in a dimensionless velocity, the Reynolds number, $\Delta Re = \Delta\Omega_i R_i d/\nu$, with respect to the change in a

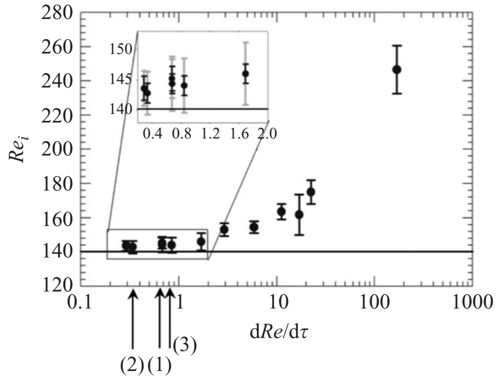

FIGURE 1. Ramp test used to determine the critical $\mathrm{d}Re/\mathrm{d}\tau$ value used in quasi-static experiments. In the subplot, the dark error bars represent experimental uncertainty, while the grey error bars represent the sum of both the experimental uncertainty and the range of *Re* between the onset of TVF (counted as formation of the third vortex from each end) and steady TVF. The solid line is the critical condition predicted by linear stability theory. Point (1) is used in these experiments as the critical dimensionless ramp rate, as it lies within the regime where there is no change of the critical condition within experimental confidence. Point (2) is the ramp rate suggested by Baxter & Andereck (1986) of $(20/\Gamma) > (\mathrm{d}Re/\mathrm{d}\tau)$, which takes into account aspect ratio effects, and point (3) is the ramp rate used by Andereck *et al.* (1986), when cast in terms of $\mathrm{d}Re/\mathrm{d}\tau$.

dimensionless time scale, $\Delta t = \Delta t/(d^2/\nu)$. The time scale is made dimensionless by the viscous time scale, d^2/ν, which is much smaller than other time scales present in the system (e.g. the time scale $= h^2/\nu$ required for the diffusion of vorticity from the ends of the cylinder and the thermal time scale $= d^2/\alpha$, where α is the thermal diffusivity).

Four Newtonian solutions of glycerin and water (7 %, 50 %, 61 % and 80 % glycerin) were used to obtain a wide range of τ and *Re* and determine the critical dimensionless ramp rate as follows. The critical condition for TVF at $Re_o = 0$ was determined as a function of ramp rate. When the critical condition approached that defined by linear stability theory and became independent of ramp rate within the measurement error, the critical dimensionless ramp rate, $(\mathrm{d}Re/\mathrm{d}\tau)_c = a_c$, was defined (figure 1). In general, the critical condition at $\mathrm{d}Re/\mathrm{d}\tau < 1$ approaches that defined by linear stability theory ($Re_c = 140.2$), but remains above the predicted value by a few percent. This predicted value of 140.2 is used to calculate $Re^* = Re_i/Re_c$. From the results shown in figure 1, a_c was assigned to 0.68. For comparison, a conservative estimation of the dimensionless ramp rate used by Andereck *et al.* (1986) is $\mathrm{d}Re/\mathrm{d}t \sim 0.8$ (based on water at 20°C and considering the viscosity increase due to the seeding particles).

We note that other researchers (Park, Crawford & Donnelly 1981; Baxter and Andereck 1986; Czarny and Lueptow 2007) have suggested a time scale of dh/ν instead of d^2/ν for non-dimensionalizing the ramp rate. Park *et al.* (1981), considering the primary transition, suggested the criterion for a quasi-non-hysteretic dimensionless ramp rate as $(\mathrm{d}Re/\mathrm{d}t) \times (dh/\nu) < 10$. However, when the ramp rates from Park *et al.* (1981) are recast in terms of $\mathrm{d}Re/\mathrm{d}\tau$, we find that the critical condition is well described by $\mathrm{d}Re/\mathrm{d}\tau < 2/3$, which is essentially identical to the condition we use. Also, Baxter and Andereck (1986) found that, for their geometry, quasi-static conditions could be found for $(\mathrm{d}Re/\mathrm{d}t) \times (dh/\nu) < 20$. Using this criterion for our geometry, the critical ramp rate would be $\mathrm{d}Re/\mathrm{d}\tau < 1/3$. However, figure 1 shows that this ramp rate does not significantly alter the critical condition. When, instead, the critical ramp rate of $(\mathrm{d}Re/\mathrm{d}t) \times (dh/\nu) < 20$ is cast in terms of $\mathrm{d}Re/\mathrm{d}\tau$ for the geometry used by Baxter and Andereck (1986), we once again see the critical ramp rate of $\mathrm{d}Re/\mathrm{d}\tau < 2/3$. The critical ramp rate used in this work, that used by Andereck *et al.* (1986) and the critical rate suggested by Baxter and Andereck of $(\mathrm{d}Re/\mathrm{d}t) \times (dh/\nu) < 20$ are indicated in figure 1.

The effect of ramp rate on higher order flow states (e.g. WVF) has been explored experimentally by Xiao, Lim & Chew (2002) with $\eta = 0.894$ and $\Gamma = 94$, who found that the wave speed and the amplitude were essentially unaffected by dimensionless ramp rates below $\mathrm{d}Re/\mathrm{d}\tau \sim 10$. Other studies, such as Baer & Gaekel (2008) and Pfister & Gerdts (1981), have explored the effect of ramping protocol on a Hopf bifurcation (e.g. to WVF). With sudden increases or decreases in Re_i, Pfister and Gerdts (1981) found a critical slowing down of the time scale associated with the formation or decay of a steady oscillation amplitude near the bifurcation point. Additionally, Baer and Gaekel (2008) studied a Hopf bifurcation with linear and nonlinear ramping protocols and found differences in the location of the critical conditions depending on whether the ramp involved acceleration or deceleration through the bifurcation. This critical slowing down suggests that a constant dimensionless ramp rate may not be the optimal strategy for determining the critical conditions near Hopf bifurcations; however, we believe that this approach is the best compromise for the present study in which we are examining a broad range of transitions, fluids and Re_o.

Unless otherwise noted, the results presented below were found using the critical ramp rate of $\mathrm{d}Re/\mathrm{d}\tau = a_c = 0.68$. The ramp is achieved by a series of small steps in angular velocity of 0.001 rotations s^{-1} (the minimum achievable with the stepper motors), where each step in angular velocity is held for an appropriate period of time. While the size of the steps in Re_i depends on the viscosity of the fluid, the critical ramp had step sizes of $\Delta Re_i < 0.6$. Others have noted that slow drifts in the control parameter can lead to alternative pathways of transitions (Sinha, Kevrekidis, & Smits 2006; Avila *et al.* 2007; Abshagen *et al.* 2008), and so care needs to be exercised in interpreting the results from these ramp experiments. We believe (based on the resolution of our stepper motors, the temperature control of the cell, etc.) that the drift is nominal over the time scale probed for the present quasi-static ramps; indeed, results shown later (figure 6) reveal the same transition pathway even with varied ramping protocols. To access the higher order flow states discussed in § 3.3 in a reasonable amount of time, a modified ramping procedure was used. The critical condition defining the onset of the flow state was measured as a function of dimensionless ramp rate $\mathrm{d}Re/\mathrm{d}\tau$, then extrapolated to $\mathrm{d}Re/\mathrm{d}\tau = a_c = 0.68$. In experiments with $Re_o \neq 0$, Re_o was established first, and then Re_i was reached through a ramp at a_c while maintaining Re_o constant.

2.3. *Flow characterization*

Changes in stability during adiabatic increases of Re_i were determined using flow visualization and spectral analysis. All flow states are characterized by symmetry/symmetry-breaking features as well as by wavenumbers in the azimuthal and axial directions. Flow visualization images of 2D spatial planes, captured at 33 ms intervals (30 fps), were collected over times of order 1–10 hr. From these image sequences, space–time plots were generated by extracting single (1D) lines of pixel intensity at a particular spatial location from sequential images.

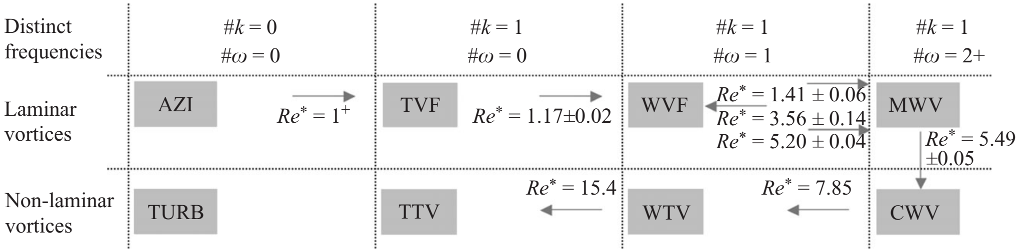

FIGURE 2. Overall sequence of transitions for a quasi-static ramp for T-C flow with $\eta = 0.912$, $\Gamma = 60.7$ and $Re_o = 0$ and generic pathway features (read clockwise starting from AZI). Errors associated with the WVF_1, MWV_1 and WVF_2 transitions are the standard deviation of the trials over all ramps from $(0.26)a_c < \mathrm{d}Re/\mathrm{d}\tau < (4.31)a_c$. The errors for MWV_2 and CWV are from the standard deviation of the trials with the typical pathway found with $\mathrm{d}Re/\mathrm{d}\tau = a_c$. $\#k$ and $\#\omega$ are the number of well-defined, distinct spatial wavenumbers and temporal frequencies, respectively, present in the flow state.

The 2D fast Fourier transforms (FFT) of small subsections of the resulting space–time plots were then taken at regular, overlapping intervals. These subsections were small enough that Re does not vary significantly, but large enough that they were several times longer than the time scale associated with the inverse of the frequency of the flow state. The plots of the complex modulus of the 2D FFT $|F(\kappa, \omega)|$, where κ and ω are the spatial and temporal frequencies, respectively, were then averaged across spatial frequencies to determine a 1D averaged dependence on temporal frequency, $< |F(\omega)| >_\kappa$. Likewise, averages across temporal frequencies produce 1D plots of the complex modulus as a function of spatial frequency ($< |F(\kappa)| >_\omega$) or spatial wavenumber ($< |F(k)| >_\omega$), where $k = 2\pi d\kappa$. These averaged complex moduli of the FFTs are then stacked as a function of Re_i (or time) to display the temporal and spatial spectral evolution of multiple flow states as the flow transitions from laminar to turbulent flow. These plots are referred to as temporal frequency–time or spatial wavenumber–time plots throughout the paper. From these frequency/wavenumber–time plots, the emergence or decay of temporal and spatial frequencies, and thus the critical condition for each flow state, can be easily identified.

The resultant spectral evolution plots are similar to those reported by Takeda (1999) for $Re^* > 7$. However, these plots have not been reported for pre-chaotic transitions or co-rotational flows. Values on the spatial wavenumber axis could be determined to within $\pm$ 4.3 %; the error is based on the spatial resolution established by the pixel size in our imaging set-up. The temporal frequency can be determined to within around $\pm$ 0.5 %; the error is based on the non-zero ramp rate and the image capture rate. In § 3, both the space–time and frequency/wavenumber–time plots are given for each flow state transition, with the corresponding 1D FFT and 2D FFT plots for each specific flow state.

3. Results and discussion

Flow state transitions with $Re_o = 0$ follow a pathway of increasing temporal frequency complexity with increasing Re_i. These observed transitions, comparisons with similar transitions in other geometries in the literature and discussions of the unique features are described in §§ 3.1–3.3. The overall quasi-static pathway is shown in figure 2, where $\#k$ is the number of well-defined, distinct spatial wavenumbers and $\#\omega$ is the number of well-defined, distinct temporal frequencies present in the flow state. This figure demonstrates the pathway's energy cascade, in which there is first an increase in the number of spatial then temporal frequencies, followed by the appearance of a broad component in the spectrum with a decrease in the number of well-defined, distinct temporal then spatial wavenumbers.

3.1. *Lower order flow transitions: Axisymmetric and non-axisymmetric laminar torodial rings*

For a stationary outer cylinder (as well as for the small range of Re_o near zero considered here), the primary instability from Couette flow (which we denote by AZI, for purely azimuthal flow) is to TVF. TVF is characterized by axisymmetric toroidal vortices that define an invariant manifold (heteroclinic orbit) with hyperbolic fixed points at the walls at intervals defined by an axial wavenumber, in which the streamlines do not cross from one ring to the adjacent ring. As more energy is added to the system, a secondary mode is excited at a second critical condition. At this transition, the heteroclinic orbit becomes a heteroclinic tangle, and fluid elements from one vortex can enter into another. This transport of fluid elements causes movement at the vortex boundaries at a unique azimuthal wave number. As noted by Coles (1965), the WVF state is part of a 'nonlinear regime of Taylor flow', so the state, defined by the axial and azimuthal wave numbers, depends strongly on the manner in which it is accessed.

The transitions from AZI to TVF to WVF are shown in figure 3 for a ramp rate of a_c and a fluid of viscous time scale $\approx$ 9.5 s. Figure 3(*a*) illustrates the evolution of the flow in the axial direction, z, over the length $\Delta z/d = 32.5$ in a space–time plot, from $Re_i = 123$ to 200. This particular plot contains information from over 30 000 sequential images of flow in the z-Θ plane. The critical condition for TVF is at $Re_i = 144 \pm 4.2$ ($Re^* = 1.03 \pm 0.03$) (compare figure 1), the transition to WVF occurs at $Re_i = 164.2 \pm 3.4$ ($Re^* = 1.17 \pm 0.00$) and the destabilization of WVF (i.e. the emergence of MWV_1) occurs at $Re_i = 198.3 \pm 8.6$ ($Re^* = 1.41 \pm 0.06$). While the ramp rate dependence of TVF is shown in figure 1 and the critical condition is reported for a ramp rate of a_c, the transitions to WVF_1 and MWV_1 were found to be independent of ramp rate for the range of $(0.26)a_c < \mathrm{d}Re/\mathrm{d}\tau < (4.31)a_c$ (discussed below, figure 8). The given critical conditions and error for these later transitions are from the average and standard deviation from experiments conducted over this range of ramp rates. Figures 3(*b*) and 3(*c*) show the development of the temporal frequencies and spatial wavenumbers, respectively, of the flow in figure 3(*a*) with Re_i. Sets of 2D FFT, 1D $<|F(\omega)|>_k$ and 1D $<|F(k)|>\omega$ are shown in figures 3(*d–f*), 3(*g–i*) and 3(*j–l*) for $Re_i = 175$, 155 and 135, respectively, corresponding to WVF, TVF and AZI.

The frequency associated with the inner cylinder rotation (due to slight azimuthal variations in the anodization of the inner cylinder that produce changes in the intensity of the reflected light as the cylinder rotates) can be seen even in the purely azimuthal flow and is observed for all Re_i, independent of the flow state. The frequency from the inner cylinder rotation is denoted in the 1D $<|F(\omega)|>_k$ figures with an asterisk, '*' (e.g. figure 3*e*,*h*,*k*). It should be noted that typically when the frequency of cylinder rotation is observed by others (e.g. Andereck *et al.* 1983, 1986; Zhang & Swinney 1985) in the power spectrum, it is also attributed to light reflection artefacts, as it is here. These artefacts may arise due to azimuthal optical variations in the cylinders (e.g. uneven anodization) or may be due to some nominal degree of eccentricity. However, the presence of the frequency even in the purely azimuthal flow suggests that this frequency, along with any harmonics, is not associated with the flow state.

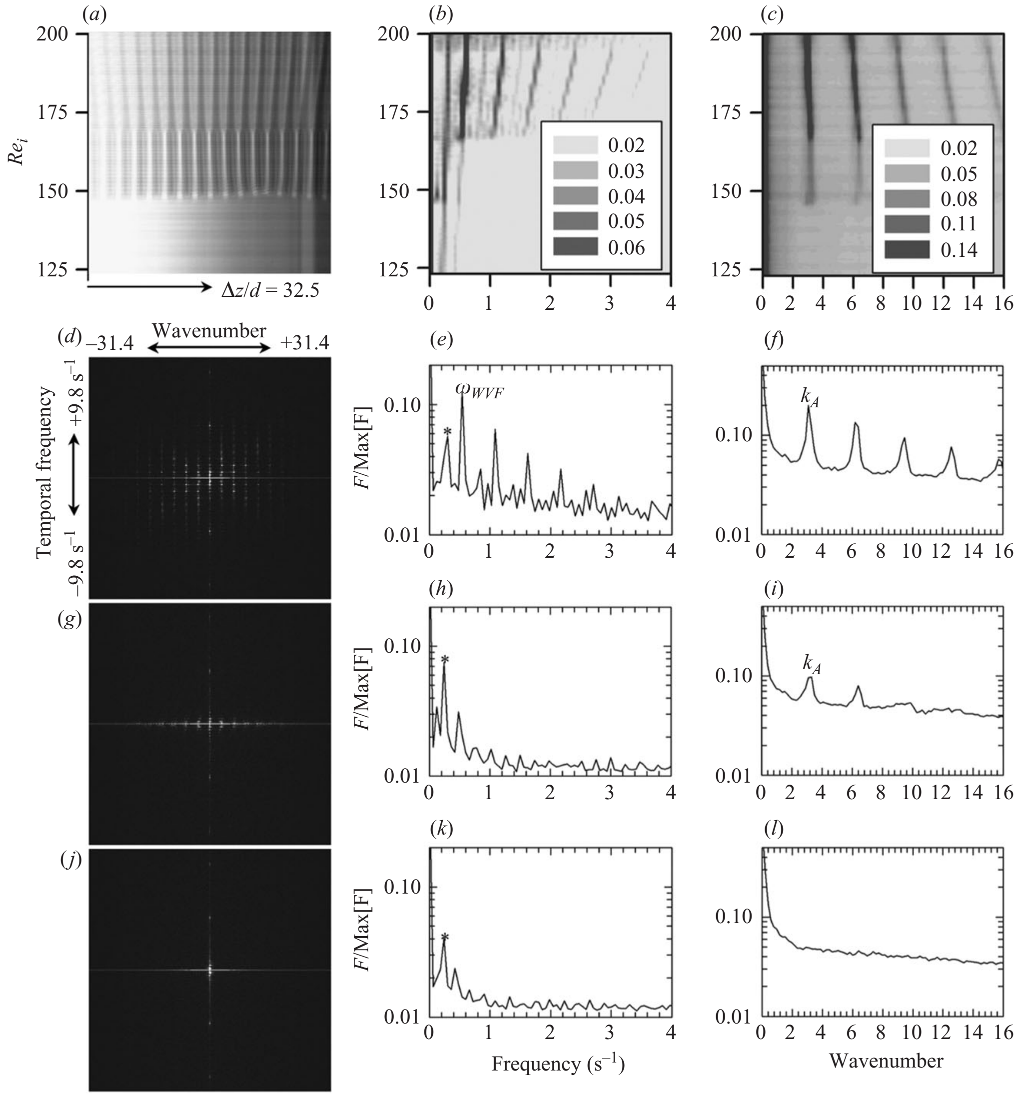

FIGURE 3. Transitions from AZI to TVF to WVF_1 to the cascade region within MWV_1. The frequency associated with the inner cylinder rotation can be seen even in the purely azimuthal flow and is observed throughout for all Re_i, independent of the flow state, and is denoted by '*'. The transitions are shown in a space–time plot (*a*), temporal frequency–time plot (*b*) and a spatial wavenumber–time plot (*c*), where the grey contours represent the magnitude of the complex modulus of the FFT, F, normalized by the maximum value (Max[F]) at each value of time or, equivalently, Re_i. Sets of 2D FFT, 1D averaged temporal frequencies, $<|F(w)|>_k$, and 1D averaged spatial wavenumbers, $<|F(k)|>_\omega$, are shown in (*d–f*), (*g–i*) and (*j–l*) for $Re_i = 175$, 155 and 135, respectively. Figure 3(*d–f*) shows an example of WVF, (*g–i*) of TVF and (*j–l*) of AZI. All plots are for $Re_o = 0$ and a ramp rate of a_c. Note that '*', k_A and ω_{WVF} are the spatial wavenumber or temporal frequencies associated with the inner cylinder rotation, axial periodicity and azimuthal wave for WVF_1, respectively.

The wavenumber associated with the axial periodicity of the flow, k_A, becomes evident at the onset of TVF, and can be seen along with harmonics in spatial wavenumber plots above $Re^* = 1$ (figure 3*e,f,i*). The low temporal frequency peak seen in figure 3(*b*) for a small range of Re_i near the onset of TVF is that associated with the initial arrangement of the Taylor vortices. In all experiments at the critical ramp rate a_c, axisymmetric Taylor vortices become fully formed and this temporal frequency vanishes prior to any subsequent transitions. In the formation of wavy vortex flow, a temporal frequency and its harmonics develop (figure 3*b*,*e*), denoted by ω_{WVF}. Also, after the onset of WVF, the dominant spatial wavenumber decreases monotonically with Re_i, indicating a smooth growth of vortex size (figure 3*c*).

3.2. *Oscillations between wavy and early-modulated wavy flows*

As Re_i is increased further, WVF is supplanted by a state we denote by MWV_1, corresponding to either (i) the broadening of the spectral peak associated with a single dominant temporal frequency (compare figure 3*e* and figure 4*e*) or (ii) the appearance of multiple distinct dominant temporal frequencies. Figure 4 shows space–time, frequency–time and wavenumber–time plots obtained at a ramp rate of a_c for a fluid of viscous time scale ≈ 9.5 s, similar to those shown for a lower range of Re_i in figure 3, for the transition to MWV_1. Figures 4(*d*–*f*), 4(*g*–*i*) and 4(*j*–*l*) for $Re_i = 300$, 250 and 200, respectively, show an example of fully formed MWV_1 (*d*–*f*), the cascade region (*g*–*i*) and the onset of the cascade region (*j*–*l*). The onset of the cascade region displays clear spectral differences from WVF, as can be seen by comparing figure 4 (*j*–*l*) at $Re_i = 200$ with figure 3(*d*–*f*) at $Re_i = 175$. The cascade region will be defined more fully below. A transition to MWV_1 is evident at $Re_i = 198.3 \pm 8.58$ ($Re^* = 1.41 \pm 0.06$) for all ramp rates in the range $(0.26)a_c < \text{d}Re/\text{d}\tau < (4.31)a_c$. The critical condition of $Re^* = 1.41$ is in good agreement with a transitional Re^* reported by Donnelly *et al.* (1980) of 1.35 (for $\eta = 0.876$ and $\Gamma = 80$), who also reported spectral peak broadening. In the transition to MWV_1, we find from the space–time plot (figure 4*a*) that the phase of WVF unlocks prior to the peak in spatial wavenumber broadening and dislocation occurrences, similar to the phase unlocking described by Andereck *et al.* (1986) prior to the onset of MWV in the counter-rotating regime. This MWV flow regime has not been previously reported for $Re_o = 0$.

We define the cascade region of MWV_1 as having a temporal spectrum capturing both MWV_1 features coupled with a smooth, nearly continuously decaying profile (figures 4*h* and 4*k*). From figures 4(*b*) and 4(*h*) a dominant temporal frequency is still evident in this cascading regime of MWV_1. The location of the dominant temporal peak, ω_W, cascades through a series of steps to higher temporal frequencies with increasing Re_i, from the frequency associated with WVF_1 to that of WVF_2. Examples of these steps in dominant temporal frequency from ω_{WVF} to ω_W to ω_{WVF2} can be seen in figures 4(*k*), 4(*h*) and 4(*e*) for $Re_i = 200$, 250 and 300, respectively. This cascade occurs in the same regime where Park and Crawford (1983) and Ahlers *et al.* (1983) saw changes in axial wavenumber. The events these authors describe seem similar in nature to those reported in figures 4(*a*–*c*) and 4(*g*–*i*), where there is a broadening of the temporal spectral peak and spatial rearrangement occurs.

After $Re^* \sim 1.94$ ($Re_i \sim 270$), a higher azimuthal wavenumber emerges, which is associated with WVF_2, and is stabilized until $Re^* = 5.49$ ($Re_i = 770$). This transition at $Re^* \sim 1.94$ is near to that reported by Donnelly *et al.* (1980) of $Re^* \sim 2.1$, although instead of observing a WVF state again, we see that the additional temporal frequency associated with a modulation remains. Donnelly *et al.* (1980) reported that dislocations drove their observed transitional flow regime that separated the WVF regimes, and they did not report a stabilized modulated frequency. We note that the early-modulated flow state seen in the present work can occur both with and without dislocations. The modulation of a periodic variation of the wave amplitude can occur both with and without a secondary wave.

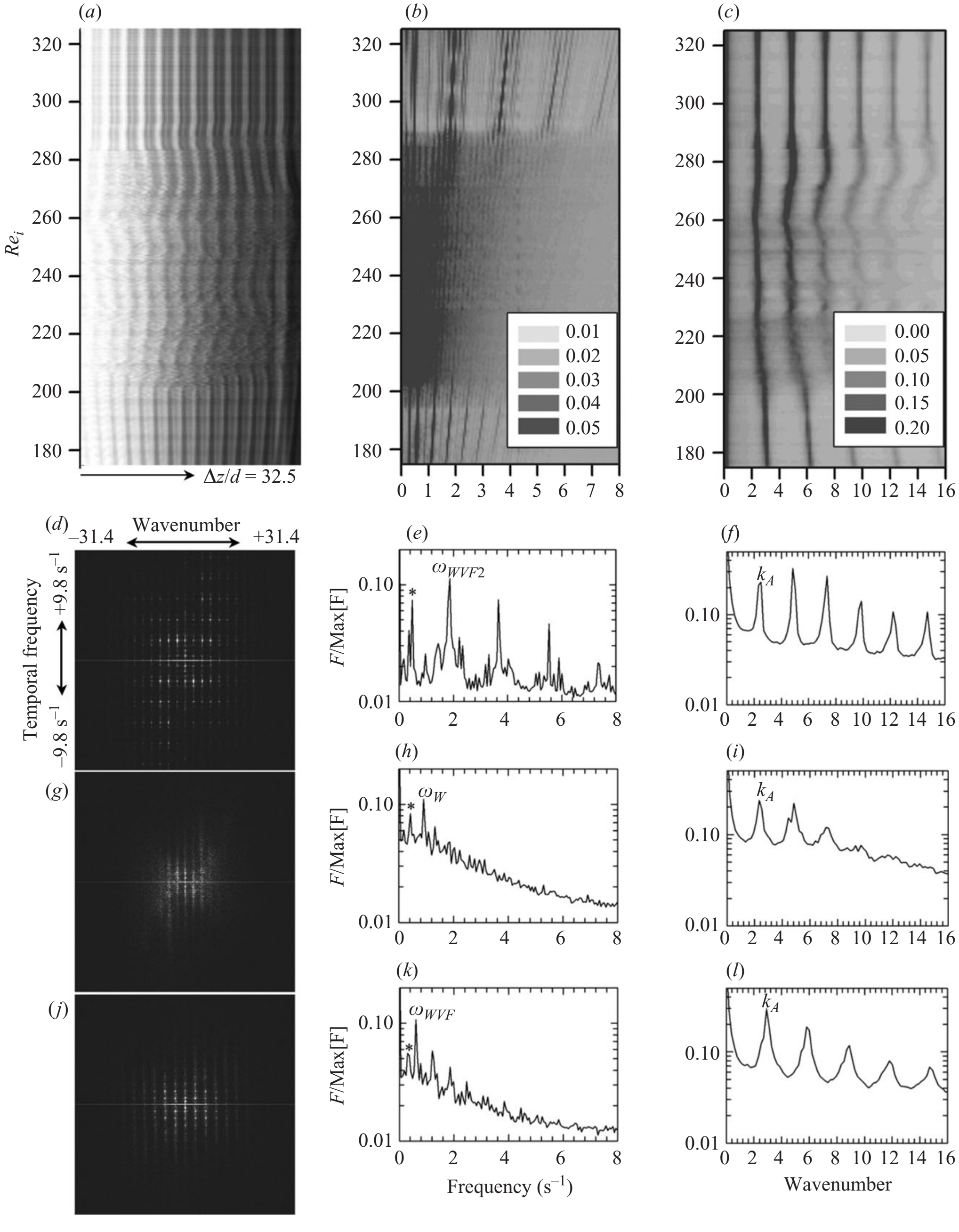

FIGURE 4. Transition from WVF to MWV$_1$. The transition is shown in a space–time plot (a), temporal frequency–time plot (b) and a spatial wavenumber–time plot (c), analogous to those in figure 3. Sets of 2D FFT, 1D averaged temporal frequencies, $<|F(\omega)|>_k$, and 1D averaged spatial wavenumbers, $<|F(k)|>_\omega$, are shown in (d–f), (g–i) and (j–l) for $Re_i = 300$, 250 and 200, respectively. Figure 4(d–f) shows an example of fully formed MWV$_1$, (g–i) of the cascade region and (j–l) at the onset of the cascade region. All plots are for $Re_o = 0$ and ramp rate of a_c. Note that k_A, '*', ω_W, ω_{WVF} and ω_{WVF2} are the spatial wavenumber or temporal frequencies associated with the axial periodicity, inner cylinder rotation and dominant azimuthal wave observed at $Re_o = 250$ or associated with WVF and WVF$_2$, respectively.

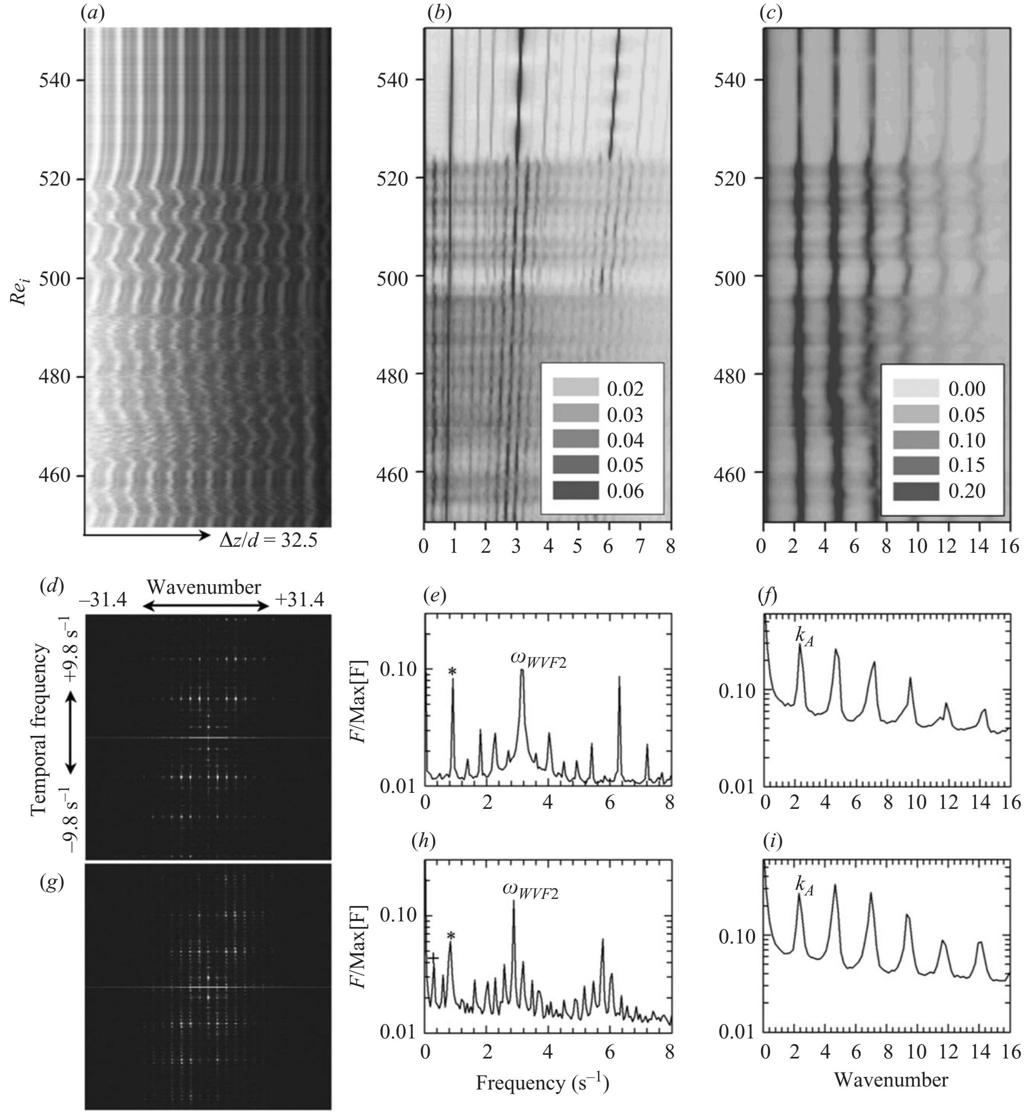

FIGURE 5. Typical transition from MWV_1 to WVF_2. The transitions are shown in a space–time plot (*a*), temporal frequency–time plot (*b*) and a spatial wavenumber–time plot (*c*), analogous to those in figure 3. Sets of 2D FFT, 1D averaged temporal frequencies, $<|F(\omega)|>_k$, and 1D averaged spatial wavenumbers, $<|F(k)|>_\omega$, are shown in (*d–f*) and (*g–i*) for $Re_i = 550$ and 500, respectively. Figure 5(*d–f*) shows an example of WVF_2 (*g–i*) of MWV_1. All plots are for $Re_o = 0$ and ramp rate of a_c. Note that k_A, '*', '+' and ω_{WVF2} are the spatial wavenumber or temporal frequencies associated with the axial periodicity, inner cylinder rotation, amplitude modulation seen in MWV_1 and a dominant azimuthal wave seen in WVF_2, respectively.

At still higher Re_i, figure 5 shows space–time, frequency–time and wavenumber–time plots obtained at a ramp rate of a_c for the MWV_1 regime and the transition from MWV_1 to WVF_2. This transition from MWV_1 to WVF_2 occurs at $Re^* = 3.56 \pm 0.14$ ($Re = 498.5 \pm 19.0$) for all ramp rates in the range $(0.26)a_c < \mathrm{d}Re/\mathrm{d}\tau < (4.31)a_c$. Sets of 2D FFT, 1D $<|F(\omega)|>_k$ and 1D $<|F(k)|>\omega$ are shown in figures 5(*d–f*) and 5(*g–i*) for $Re_i = 550$ and 500, respectively, corresponding to WVF_2 and MWV_1. It is also clear from both the space–time plots and the spatial wavenumber–time plots of figures 5(*c*) and 5(*i*) that a single dominant spatial wavenumber is possible within MWV_1. Even long after the recovery from a dislocation, a modulated wave of a low temporal frequency is clear in MWV_1 (compare figure 5*h* for MWV_1 with a low temporal frequency associated with the modulation, denoted by "+", with figure 5(*e*) for WVF_2 with no modulated temporal frequency).

From the literature, it is thought that the mixed-mode states, like that seen in MWV_1, could be related to either transients associated with the height of the cell (through a time scale h^2/ν) or the competition between the many modes allowed by the long geometry (King & Swinney 1983). An argument can be made for the stability of the mixed-mode states from the description from Donnelly *et al.* (1980) of the broadening of the power spectra as 'a persistent feature of the flow'. While the ramp protocol was not reported by Donnelly *et al.* (1980), it was reported that the transitional flow state persisted even when waiting for a time that was long compared with the end effect time scale $0.15h^2/\nu$ suggested by Snyder (1969). Also, while most of their observations of distorted wave patterns were discussed for $\Gamma > 32$, King and Swinney (1983) do observe 'persistent distorted wave patterns even for $\Gamma \leqslant 30$'. The presence of enduring mixed-mode flow in geometries with moderately smaller aspect ratios again supports the argument that the distorted WVF pattern is a stable state that corresponds to a mixed-mode solution rather than a transient state associated with long geometries.

In order to elucidate the stability of this early MWV_1 mode, the flow state was accessed using a wide range of ramp rates. If MWV_1 is a transient state associated with the height of the cell (through a time scale h^2/ν), then the Re_i range of stability would scale proportionally to the dimensionless ramp rate used. Figure 6 shows the range of stability for MWV_1 in temporal frequency–time plots for $150 < Re_i < 650$ accessed with the critical ramp rate, a_c (*a–d*), and with ramp rates that varied over an order of magnitude (*e–h*). Figure 6(*a–d*) shows the typical variation in the stability range for the same ramp rate. Here, for a ramp rate of a_c, the transition from WVF_1 to MWV_1 occurs at $Re^* = 1.43 \pm 0.03$ and the transition from MWV_1 to WVF_2 occurs at $Re^* = 3.59 \pm 0.10$ ($Re_i = 503.5 \pm 13.9$), leading to a range of stability for MWV_1 of $\Delta Re_i = 303.2 \pm 14.4$. A non-monotonic, and comparable, variation of the transitions is also present in experiments that differed in ramp rate by a factor of 16.6 (figure 6*e–h*). Here, the transition from WVF_1 to MWV_1 occurs at $Re^* = 1.41 \pm 0.06$ and the transition from MWV_1 to WVF_2 occurs at $Re^* = 3.56 \pm 0.14$ ($Re_i = 498.5 \pm 19.0$), leading to a range of stability for MWV_1 of $\Delta Re_i = 300.3 \pm 20.8$. The slowest ramp used, of $0.26a_c$, (figure 6*h*), corresponds to a series of very small steps in Re_i during which Re_i is held constant for several ($\sim$3.3) viscous time scales. The MWV_1 stability thus appears to be independent of ramp rate and cannot be made to vanish with a sufficiently slow ramp, which indicates that MWV_1 is not a transient flow state.

The broadening of the spectrum seen in the cascade region (described by Ahlers *et al.* 1983; Park and Crawford 1983) admittedly does experience some decay with decreasing ramp rate, although the stability range of the cascade regime decreases only by a factor of $\sim$2.5. In all cases, the dominant frequency cascade is still evident across ramps and a stabilized MWV_1 both with and without dislocations occurs. It should be noted that with the slowest ramp rate, $\mathrm{d}Re/\mathrm{d}\tau = (0.26)a_c$, the first transition occurred with defects in the TVF structure. In order to start from the same TVF structure as with other ramps, the ramp shown in figure 6(*h*) was achieved by first ramping past the primary transition with a critical ramp rate, a_c, to $Re_i = 155$,

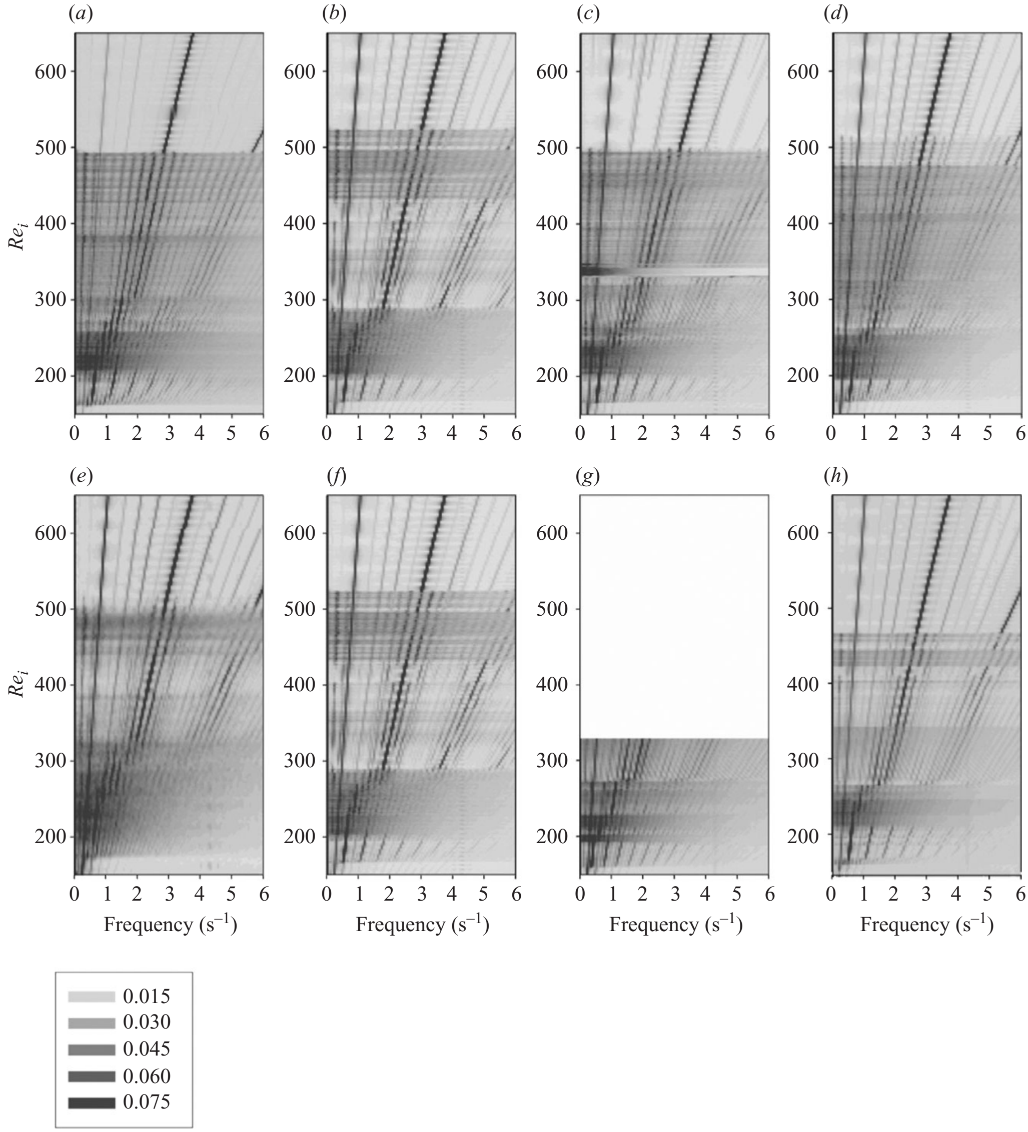

FIGURE 6. Typical temporal frequency–time plots for the same (*a–d*) and various ramp rates (*e–h*). The ramp rates are (*a–d*) $\mathrm{d}Re/\mathrm{d}\tau = a_c$, (*e*) $\mathrm{d}Re/\mathrm{d}\tau = (4.31)a_c$, (*f*) $\mathrm{d}Re/\mathrm{d}\tau = a_c$, (*g*) $\mathrm{d}Re/\mathrm{d}\tau = (0.43)a_c$, (*h*) $\mathrm{d}Re/\mathrm{d}\tau = (0.26)a_c$, where (*b*) and (*f*) are the same experiments. The grey contours represent the magnitude of the complex modulus of the FFT, F, normalized by the maximum value (Max[F]) at each value of Re_i. The white region represents a region where no data were recorded.

then slowing the ramp to the $\mathrm{d}Re/\mathrm{d}\tau = (0.26)a_c$ rate. In this way, the transitions of interest (WVF to MWV_1 to WVF_2) could be accessed from the same starting flow state.

MWV_1 seems different from the early non-propagating oscillatory mode presented by Zhang & Swinney (1985) for $\eta = 0.883$, $10 < \Gamma < 50$ within the range of $3 < Re^* < 10$, where they report occurrences of a non-periodic stationary mode. Instead, based on our flow visualization and spectral analysis, the flow state seen here parallels the early modulation that has been reported in the counter-rotating regime by Andereck *et al.* (1986). This novel stabilization of early-modulated waves seems to represent the superposition of multiple wavy modes competing for stability.

Like Andereck *et al.* (1986), we also see early MWV in the counter-rotation plane, demonstrated in a temporal frequency–time plot in figure 7 for $Re_o = -27$. Unlike Andereck *et al.*, we found that MWV_1 was stabilized for $Re_o = 0$ (figure 7*b*), indicating that our different geometry may allow the envelope of MWV_1 stability on $Re_o - Re_i$ coordinates to traverse the stationary outer cylinder axis and extend into the co-rotation regime. Figure 7 is a series of temporal frequency–time plots for $125 < Re_i < 558$ and Re_o of −27, 0, 13, 30, 50, 70 and 75. It is clear from these data that the early MWV, separating WVF_1 and WVF_2 in the range of $198.3 \pm 8.6 < Re_i < 498.5 \pm 19.0$ for $Re_o = 0$, also occurs in the co-rotation regime. The range of stability separating WVF_1 and WVF_2 narrows with increasing Re_o (e.g. $177 < Re_i < 408$ for $Re_o = 30$, $190 < Re_i < 280$ for $Re_o = 50$) and disappears between $50 < Re_o < 70$. This apparent stabilization of early MWV_1 is likely due to the high aspect ratio of our geometry, since our Γ differs more significantly than our η from those of Andereck *et al.* and multiple modes can be supported by a high aspect ratio as discussed in the introduction for $Re_o = 0$ flows. Another interesting aspect of figure 7 is the stability of three distinct wavy vortex flow states for $Re_o \geqslant 50$ separated by brief cascading periods. The cascade regions seen at $Re_o = 70$ and 75 separating WVF_1, WVF_2 and WVF_3 regions are still present at $Re_o = 85$ (not shown). At $Re_o = 85$ we also observed added complexity in the form of additional modulations of temporal frequency within the WVF_3 regime.

Fuller quantitative studies based on the FFT analysis of the co-rotation regime are beyond the scope of the present work. However, we include in figure 8 a phase diagram of the entire range of $Re_i - Re_o$ accessible in our experiments based on the approximate assignment of the stability of each flow state from space–time plots. The assignment of the higher order states is consistent with the definitions of Andereck *et al.* (1986), although the stability boundaries are shifted due to the differences in η and Γ. We believe that these data will be useful in developing expressions for $Re_c(\eta, Re_o)$ for higher transitions and as a baseline for looking at the effects of additional variables (elasticity, imposed temperature gradients, magnetic fields, etc.) on flow transitions in Taylor–Couette flows.

3.3. *Higher order flow transitions: MWV_2, non-axisymmetric and axisymmetric chaotic vortices*

Returning to the $Re_o = 0$ case, at still higher Re_i, the modulation of WVF_2 begins to occur, resulting in MWV_2. This occurrence of MWV_2, where two distinct temporal frequencies are present in the flow, has been discussed extensively in the literature. The vast majority of the literature characterizing MWV_2 was performed with the geometry of $\eta \approx 0.88$, $\Gamma \approx 20$ (e.g. Gollub & Swinney 1975; Fenstermacher *et al.* 1979; Gorman & Swinney 1982; Brandstater & Swinney 1987, see table 1) and the question of the existence of MWV for other geometries was initially posed by Gorman & Swinney in 1982. Since then, stabilized regions of MWV in slightly different geometries have been reported by other researchers, such as Takeda (1999) for $\eta = 0.904$ and $\Gamma = 20$ and Meincke & Egbers (1999) for $\eta = 0.85$ and $\Gamma = 13.2$; however, MWV is not observed in smaller η experiments, such as those of Wang *et al.* (2005) with $\eta = 0.733$ and $\Gamma = 34$.

As is seen in the literature, within this MWV regime, a chaotic transition occurs (e.g. Fenstermacher *et al.* 1979), where a broad peak appears in the spectrum and

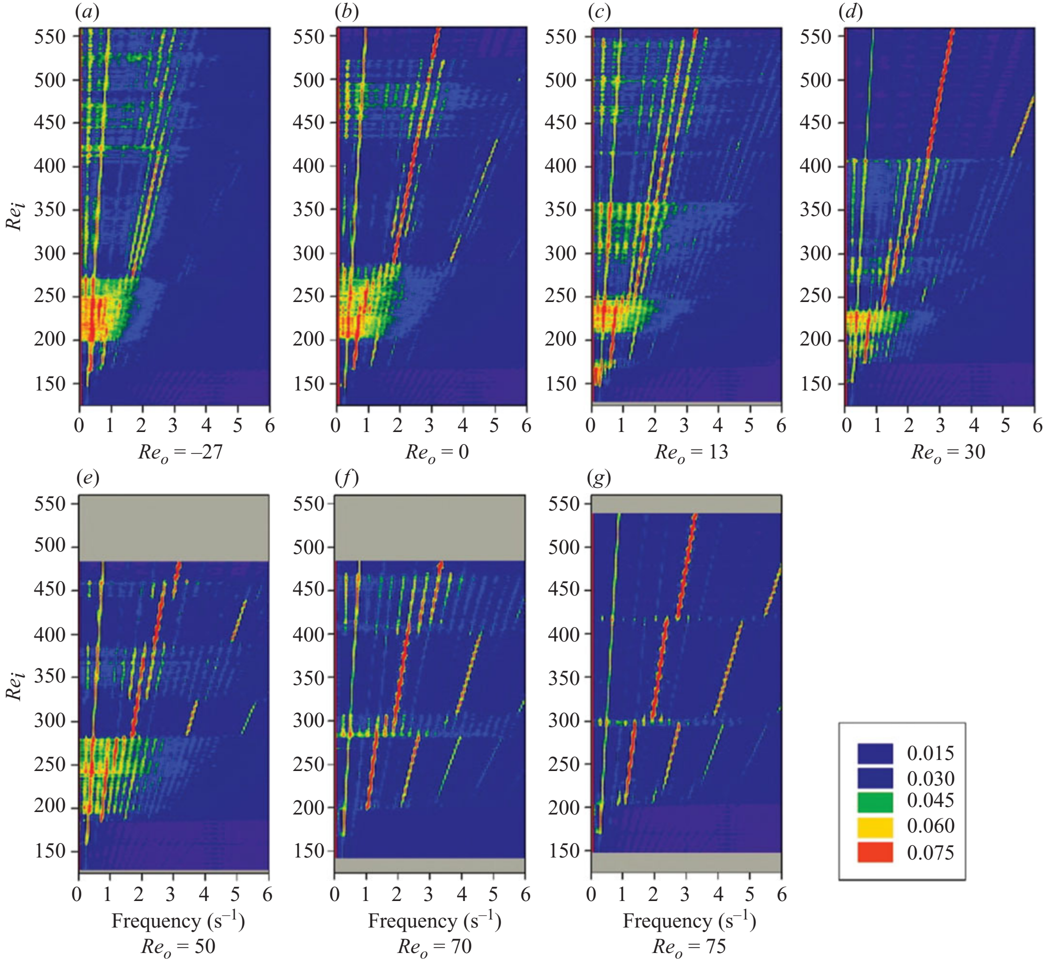

FIGURE 7. Temporal frequency–time plots describing the evolution of temporal modes for $125 < Re_i < 558$ for $Re_o = -27$, 0, 13, 30, 50, 70 and 75. The colours represent the magnitude of the complex FFT, F, normalized by the maximum value (Max[F]) at each value of Re_i. Grey regions represent unexplored space.

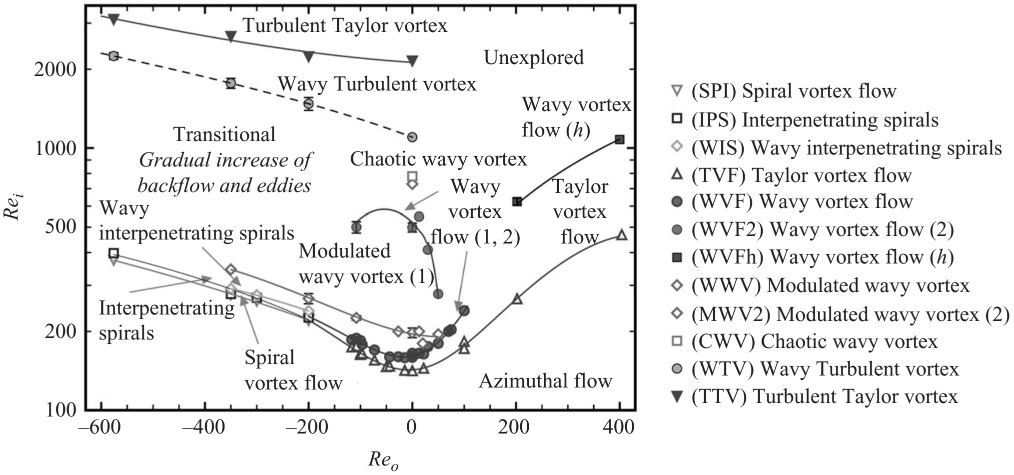

FIGURE 8. Newtonian Taylor–Couette flow stability map for radius ratio 0.912 and aspect ratio 60.7. Dashed lines indicate a gradual transition boundary. High Re_i for the co-rotation regime was not explored. Transitions with $Re_o < -50$ where determined through visual inspection of the fluid motion and space–time plots, instead of the detailed spectral analysis used to identify all other transitions.

there is an increase in the background noise. Using the notation from Takeda (1999), this new flow state is referred to here as a chaotic wavy vortex flow (CWV). Whereas MWV is defined as having multiple temporal modes, CWV is defined as having multiple temporal modes with the addition of the presence of backflow, small-scale features and a broad spectral profile. Figure 9 shows space–time (*a*), frequency–time (*b*) and wavenumber–time (*c*) plots obtained at a ramp rate of a_c, for the transitions from WVF$_2$ to MWV$_2$ to CWV. Figures 9(*d–f*), 9(*g–i*) and 9(*j–l*) for $Re_i = 800$, 750 and 700, respectively, show an example of CWV (*d–f*), MWV$_2$ (*g–i*) and WVF$_2$ (*j–l*). The largest unlabelled peak observed in figures 9(*k*) and 9(*h*) is a harmonic of the frequency associated with the inner cylinder rotation, denoted by '*'. The transition to MWV$_2$ occurs at $Re_i = 730 \pm 5.6$ ($Re^* = 5.2 \pm 0.04$) and CWV at $Re_i = 769.7 \pm 7.0$ ($Re^* = 5.49 \pm 0.05$). We find that for our geometry, MWV$_2$ by itself, with no additional chaotic flow transition, is stable only for the small range of $\Delta Re_i = 39.7 \pm 9.0$ ($\Delta Re^* = 0.29 \pm 0.06$).

Figure 9(*b*) shows the temporal frequency–time plot for the typical pathway through the MWV$_2$ regime. The excited modulated mode in MWV$_2$ appears as a periodic variation of the wavy amplitude. A less typical pathway was also found, where the transitions to MWV$_2$ and CWV occur at $Re_i = 805 \pm 7.1$ ($Re^* = 5.74 \pm 0.05$) and $Re_i = 879.5 \pm 17.7$ ($Re^* = 6.27 \pm 0.13$), respectively. The less typical pathway delays the MWV$_2$ and CWV transitions, and the excited MWV mode is one having double azimuthal waves. Here, the modulated frequency is lower than that seen with the typical pathway. Evidence of the dynamics in the pathway preceding the typical pathway and the less typical pathway are shown in figures 6(*a,b,d*) and figure 6(*c*), respectively. Figure 6(*c*) shows the stabilization of a higher ω_{WVF2} than that found with the typical pathway in figure 6(*a,b,d*).

Following the onset of CWV, all ramps have the same pathway and critical conditions, to WTV and TTV. Starting at the CWV transition, the bifurcations that occur at high Re_i are dominated by the presence of small-scale features. As

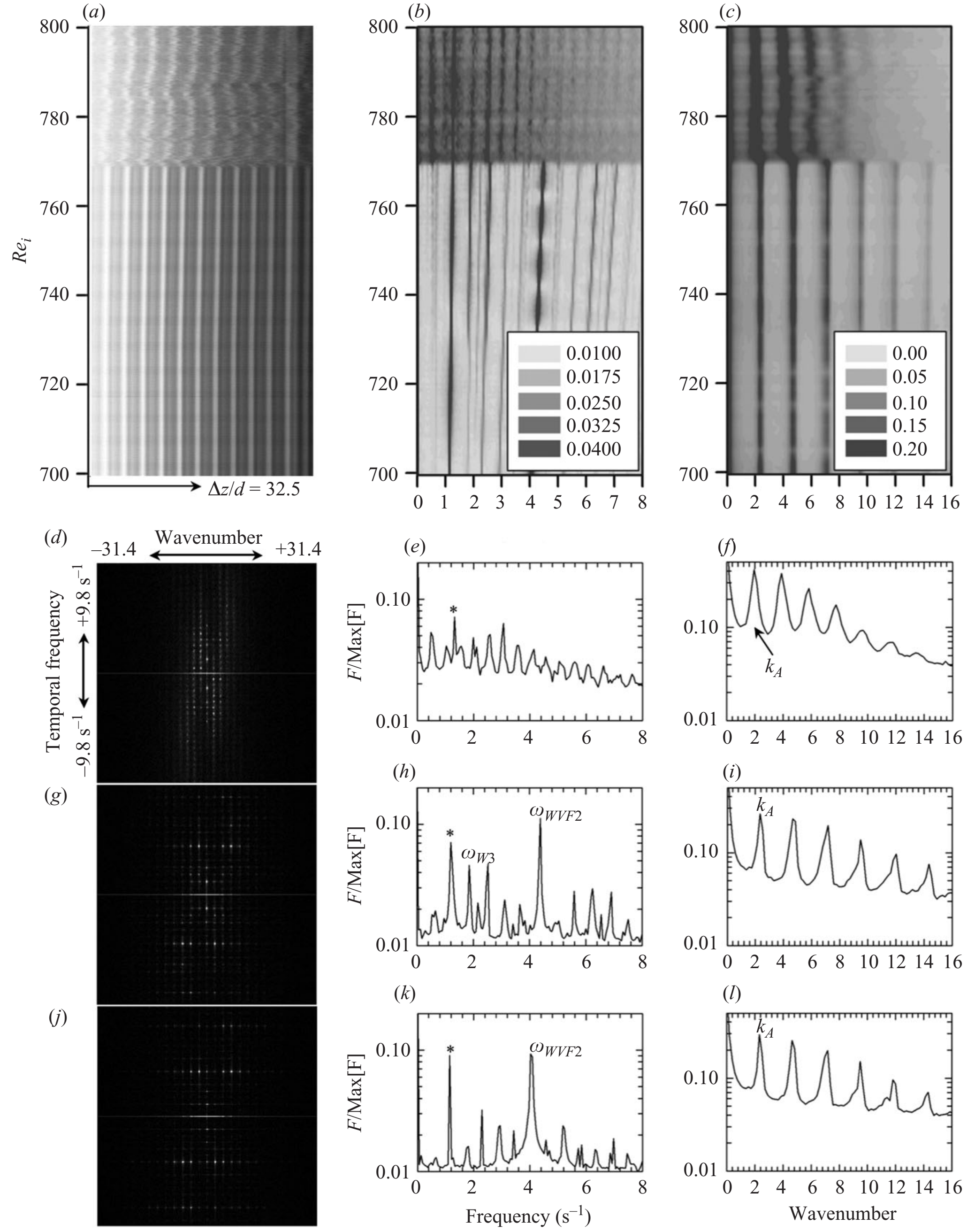

FIGURE 9. Typical transitions from WVF_2 to MWV_2 to CWV. The transitions are shown in a space–time plot (*a*), temporal frequency–time plot (*b*) and a spatial wavenumber–time plot (*c*), analogous to those in figure 3. Sets of 2D FFT, 1D averaged temporal frequencies, $<|F(\omega)|>_k$, and 1D averaged spatial wavenumbers, $<|F(k)|>_\omega$, are shown in (*d–f*), (*g–i*) and (*j–l*) for $Re_i = 800$, 750 and 700, respectively. Figure 9(*d–f*) shows an example of CWV, (*g–i*) of MWV_2 and (*j–l*) of WVF_2. All plots are for $Re_o = 0$ and ramp rate of a_c. Note that k_A, '*', ω_{W3} and ω_{WVF2} are the spatial wavenumber or temporal frequencies associated with the axial periodicity, inner cylinder rotation, modulated wave seen in MWV_2 and the dominant azimuthal wave seen in WVF_2, respectively.

energy is dissipated to this scale, the series of bifurcations that transpire have the large-scale characteristics of the primary series of transitions, but in descending order (see figure 2). For example, CWV is analogous to the laminar state of MWV. Likewise, as WVF was defined as a heteroclinic tangle with one dominant azimuthal mode, here we define WTV as having the same large-scale features as WVF, along with the addition of chaotic motion within the vortex. WTV occurs at $Re^* \sim 7.85$, where the temporal frequency associated with WTV becomes dominant (compare figures 10*e* and 10*g*). TTV, a turbulent state with the appearance of vortices, is triggered around $Re^* \sim O(10)$. This state has bulk axisymmetry, as with TVF, with small-scale chaotic motion occurring within the vortex structure.

The transitions from CWV to WTV to TTV are shown in frequency–time and wavenumber–time plots in figure 10(*a*,*b*). Unlike figures 3–9, figure 10 was obtained using a non-critical ramp rate of $\mathrm{d}Re/\mathrm{d}t = (8.62)a_c$. Figures 10(*c*–*d*), 10(*e*–*f*) and 10(*g*–*h*) for $Re_i \cong 3000$, 2000 and 1000, respectively, show an example of TTV (*c*–*d*), WTV (*e*–*f*) and CWV (*g*–*h*). The largest unlabelled peak observed in figure 10(*c*,*e*,*g*) is a harmonic of the frequency associated with the inner cylinder rotation, denoted by '*'. In the CWV state, both the temporal frequency that will later dominate WTV and a modulated frequency (and harmonics) are present. In WTV, only the wavy frequency ω_{WVF} is clearly dominant, and in TTV, no distinct temporal frequencies are maintained (except that from the inner cylinder and its harmonic, observable at all Re_i). In figure 10(*b*, *f* and *h*), it can be seen that as the flow transitions from CWV to WTV, the spatial wavenumber associated with the axial periodicity is clarified and persists through TTV. While figure 10 reveals the general features of the higher order flow states, further experiments were performed at varied ramp rates to determine the critical conditions.

To access WTV and TTV in a reasonable amount of time, a modified ramping procedure was used. The critical condition defining the onset of the flow state was measured as a function of dimensionless ramp rate $\mathrm{d}Re/\mathrm{d}t$, then extrapolated to $\mathrm{d}Re/\mathrm{d}\tau = a_c$. Figure 11(*a*–*h*) shows temporal frequency–time plots, processed as in figures 3–7 and 9–10, for a range of ramp rates from $330a_c$ to a_c to show the dependence of the flow transitions on acceleration. To determine the onset and the decay of the WTV state, the frequency–time plots in figure 11(*a*–*h*) were normalized by the magnitude of the WTV frequency (ω_{WTV}) at every Re_i; subsections of the resulting plots are shown in figure 11(*i*–*p*). The onset of WTV, identified through the growth of the peak at ω_{WTV}, is less abrupt than other transitions and the critical condition is estimated as $Re^* \sim 7.85$ ($Re_i \sim 1100$). The transition to TTV is significantly clearer, as the ω_{WTV} peak disappears suddenly. The sudden loss of this frequency is evident by the obvious transition from colour-coded values ∼0.3 to values ∼1.0 (for example, $Re_i = 2145$ in figure 11*o*).

The spectral analysis used for the majority of the transition characterization is not appropriate for very large ramp rates ($\mathrm{d}Re/\mathrm{d}\tau > 100a_c$, figure 11*a*–*c*,*i*–*k*), as the transitions occur too quickly in time to resolve clear frequency transitions. Also, the error associated with establishing a critical Re_i grows as $\mathrm{d}Re/\mathrm{d}\tau$ increases because the subplots used in the FFT analysis cover larger ranges of Re_i as the ramp rate increases. To find the TTV transition for these large ramp rates ($5000a_c > \mathrm{d}Re/\mathrm{d}\tau > 100a_c$), we manually track the movement of the midpoint between vortices in the *r*–*z* plane. As the azimuthal frequency decays, the location of the midpoint between vortices converges to a single value. Thousands of individual movie frames were analysed in random order to prevent bias in the results. The transition to TTV was defined when the midpoint between vortex centres is stationary within the measurement error.

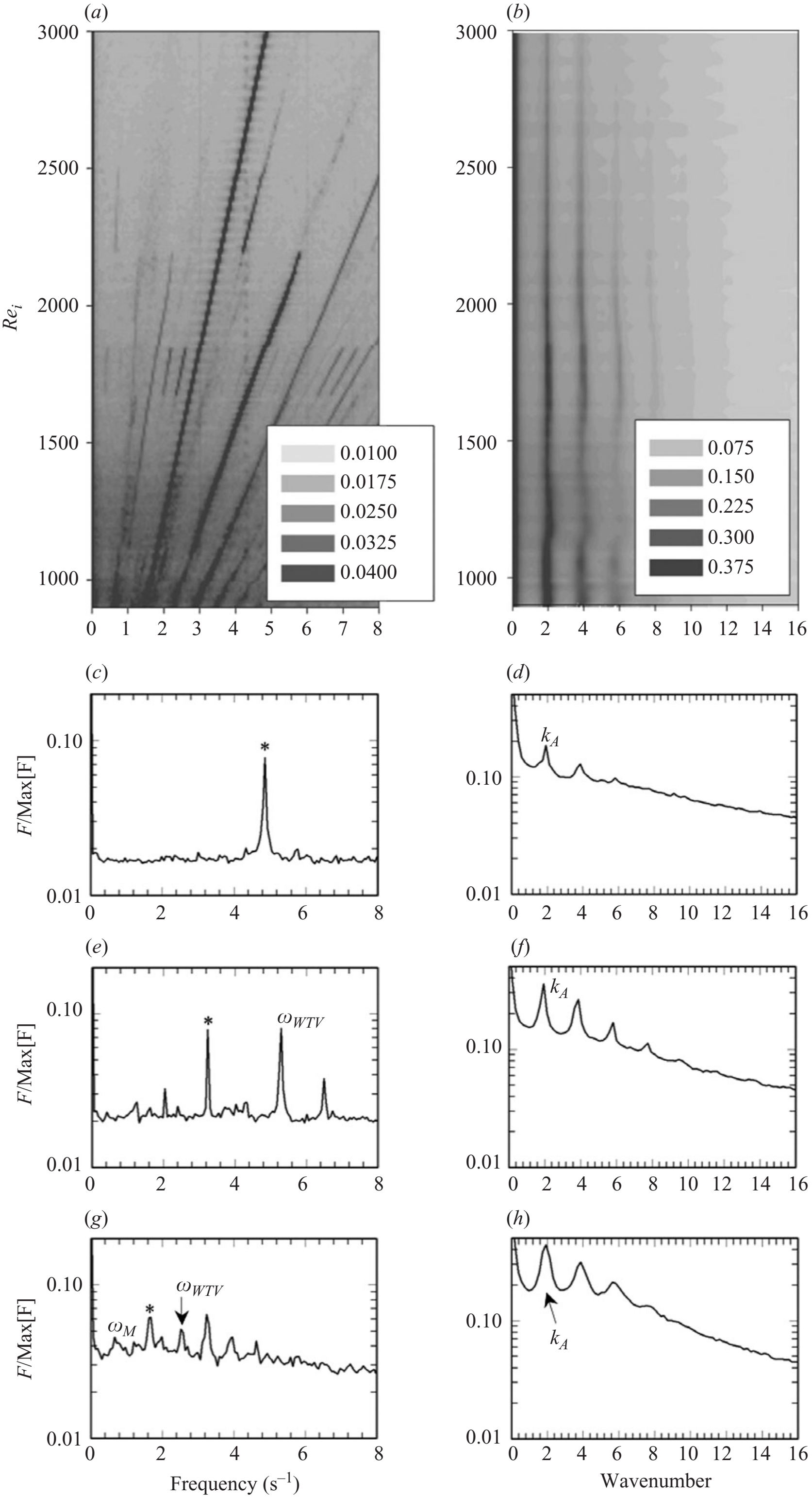

FIGURE 10. For caption see facing page.

The onset of TTV for large ramp rates can also be estimated from figure 11 (e.g. figure 13*k–o*). In figure 12, the critical conditions from the *r–z* analysis are included with those obtained from figure 11 and the delay in the critical condition for TTV with ramp rate is more pronounced. From figure 12, the critical condition for TTV was determined to be $Re_i = 2160$ ($Re^* = 15.4$). The critical condition for the TTV transition was found not to vary significantly with ramp rate for $\mathrm{d}Re/\mathrm{d}\tau < (40)a_c$. This suggests that flow states with chaotic motion within the vortices are less sensitive to the time scale defined for laminar vortices. The decrease in sensitivity may be due to the change in the characteristic length scale, L, used to define the viscous time scale, L^2/ν. For the laminar vortex states (AZI to MWV_2), L should be defined as the length separating the two moving boundaries, d. For the higher order states, L may instead be defined by the size of the small-scale features in the flow, ε. This then decreases the appropriate time scale defining the critical ramping rate to ε^2/ν, resulting in faster quasi-static ramps.

These higher order transitions have been well documented in the literature for a geometry of $\eta \approx 0.88$ and $\Gamma \approx 20$ (e.g. Fenstermacher *et al.* 1979; Gorman and Swinney 1982; Brandstater and Swinney 1987). In general, the pathway consists of a transition to MWV at $Re^* = 9$ or 10, transition to chaotic flow at $Re^* = 11$ or 12, loss of modulation at $Re^* \approx 18$ and transition to TTV at $Re^* \approx 21$. These transitions were also explored with $\eta = 0.904$, $\Gamma = 20$, $Re^* > 9$ and a modified ramping protocol, in a series of papers by Takeda *et al.* (1992, 1993) and Takeda (1999). The latter author found the coexistence of modulated and/or wavy modes up to $Re^* = 21$ as well as provided a comprehensive list of qualitative transitions in the T-C flow. MWV is reported by others at $Re^* \sim 8.5$ (Coughlin *et al.* 1991), with $\eta = 0.876$ and $\Gamma = 40$, and at $Re^* \sim 6.5$ (Meincke & Egbers 1999), with $\eta = 8.5$, $\Gamma = 13.2$. Barcilon (1979), with $\eta = 0.908$ and $\Gamma = 65$, saw 'non-unique waves' starting at $Re^* = 4.1$, WTV from $8.5 < Re^* < 20.5$ and TTV at 21 (with unreported ramping conditions). In the present work, MWV exists in the range of $5.20 < Re^* < 7.85$, CWV at $5.49 < Re^* < 7.85$, WTV at $7.85 < Re^* < 15.4$ and TTV at $Re^* > 15.4$. Based on this literature and the present results, it appears that with a longer cell and higher radius ratio, MWV and the three chaotic flow transitions occur at smaller values of Re^*. Interestingly, the stability of MWV for $\eta = 0.88$ and $\Gamma = 20$ reported by Fenstermacher *et al.* (1979), Gorman and Swinney (1982) and Brandstater and Swinney (1987) covers nearly the same region as WTV in our geometry of $\eta = 0.912$ and $\Gamma = 60.7$ ($Re^* = 9$ to 18 versus 7.85 to 15.4).

Two other notable features are seen in the present work in the higher order transitions in figure 10. First, we see the appearance and disappearance of two temporal frequencies at frequencies below ω_{WTV} in the ramp from $1700 < Re_i < 1800$ (similar in nature to MWV_2). Second, after the loss of the WTV dominant frequency, a less intense lower temporal frequency appears and later disappears in the range of

FIGURE 10. Transitions from CWV to WTV to TTV with a quick ramp of $\mathrm{d}Re/\mathrm{d}\tau = (8.62)a_c$. The transitions are shown in a temporal frequency–time plot (*a*) and a spatial wavenumber–time plot (*b*), analogous to those in figure 3. The 1D averaged temporal frequencies, $<|F(\omega)|>_k$, and 1D averaged spatial wavenumbers, $<|F(k)|>_\omega$, are shown in (*c–d*), (*e–f*) and (*g–h*) for $Re_i \cong 3000$, 2000 and 1000, respectively. Figure 10(*c–d*) shows an example of TTV, (*e–f*) of WTV and (*g–h*) of CWV. All plots are for $Re_o = 0$. Note that k_A, '*', ω_M and ω_{WTV} are the spatial wavenumber or temporal frequencies associated with the axial periodicity, inner cylinder rotation, modulated wave and dominant wave seen in WTV, respectively. The largest unlabelled peak seen in (*c*, *e*, *g*) is a harmonic of the frequency associated with the inner cylinder rotation.

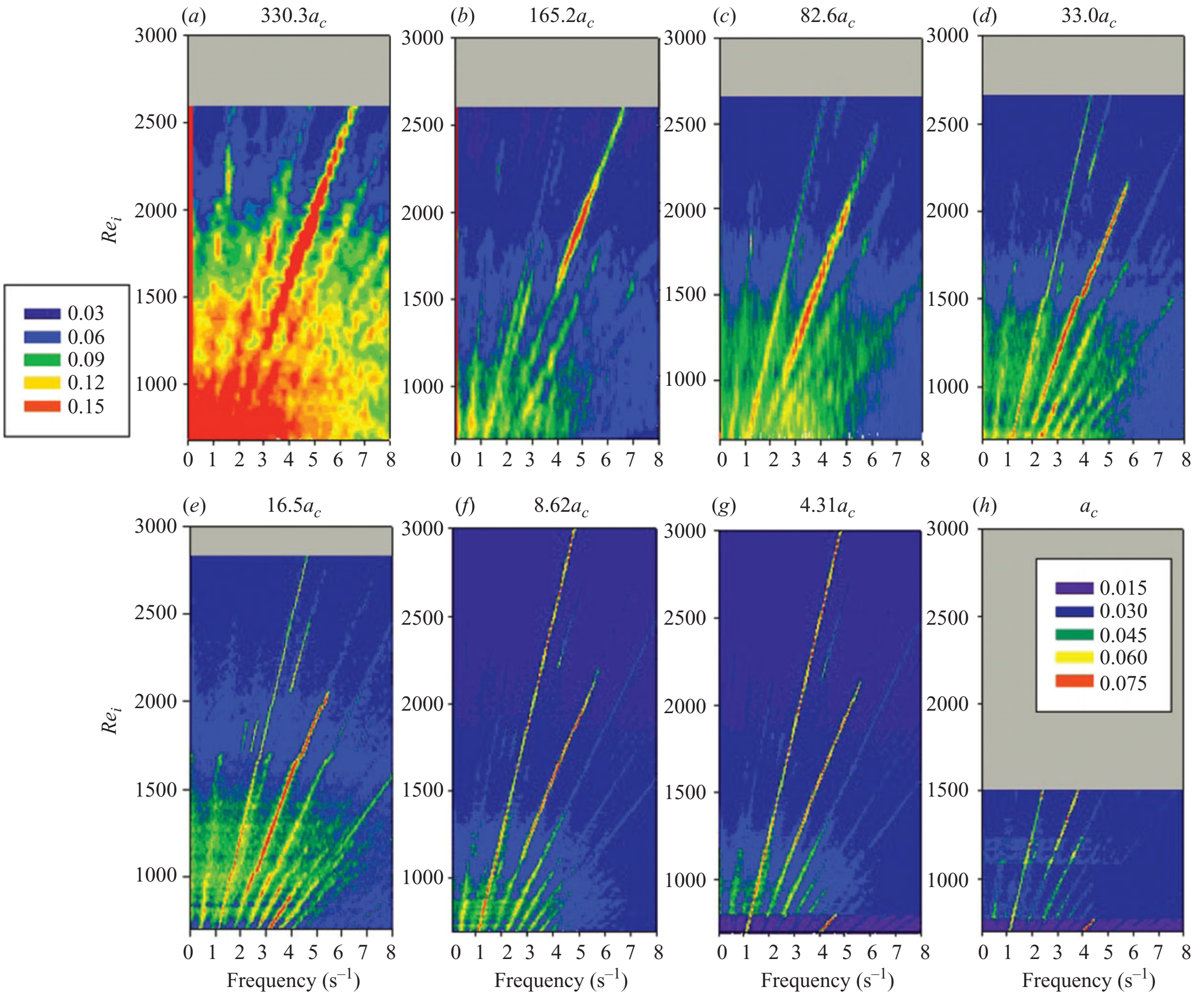

FIGURE 11. For caption see facing page.

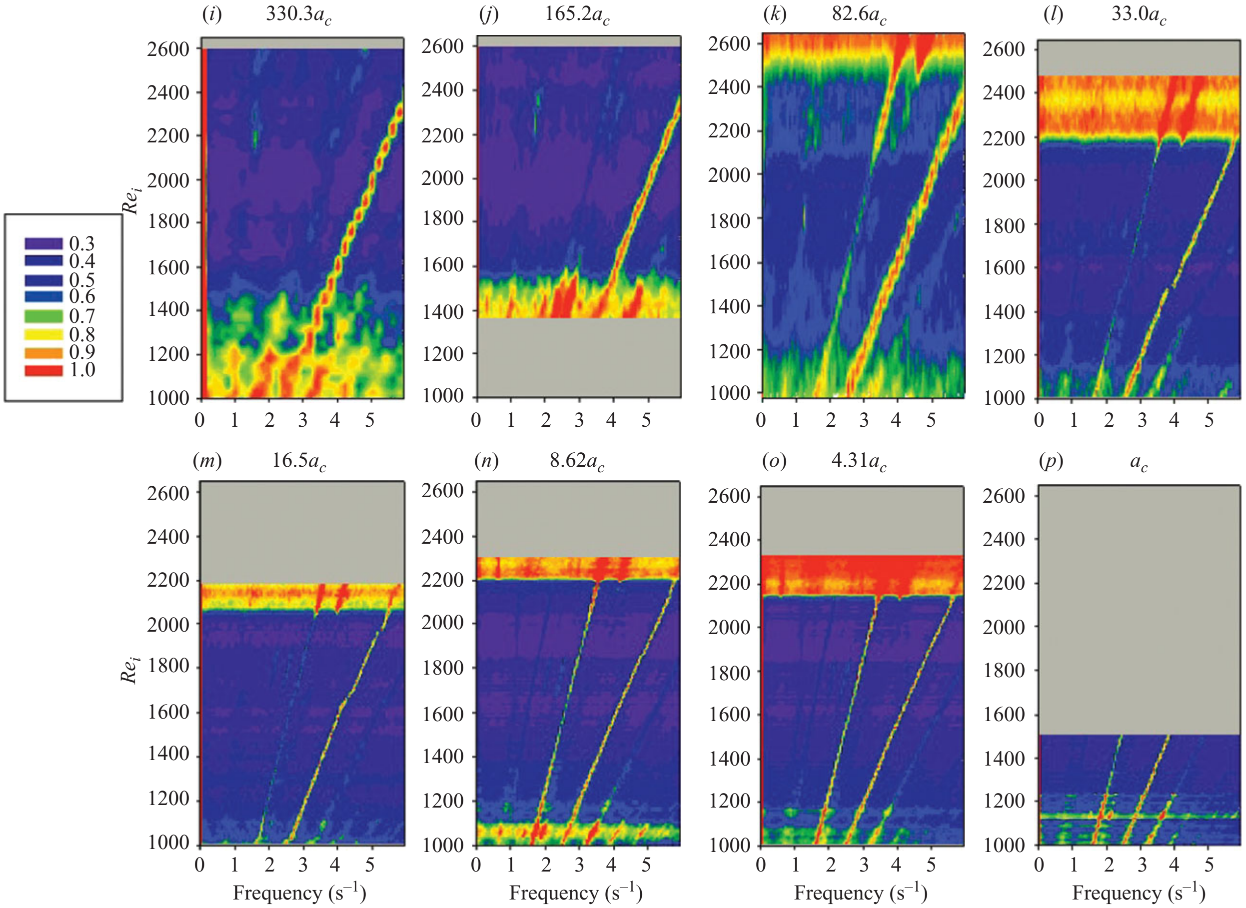

FIGURE 11. Temporal frequency–time plots describing the evolution of temporal modes for the range of ramping rates $(330.3)a_c > \mathrm{d}Re/\mathrm{d}\tau > a_c$, for (*a–h*) $700 < Re_i < 3000$ and (*i–p*) for $1000 < Re_i < 2650$. Here (*a–h*) represent standard temporal frequency–time contour plots, where the colours represent the magnitude of the complex FFT, F, normalized by the maximum value (Max[F]) at each value of Re_i. The colours are defined by the legend to the left of figure (*a*) for (*a–b*) and the legend in figure (*h*) for (*c–h*). Parts (*i–p*) are subsets of the same ramps as (*a–h*), but the colour now corresponds to the magnitude of the complex FFT, F, normalized by the complex magnitude at the WTV frequency, $<|F(\omega_{WTV})|>_k$, for each Re_i. The grey regions represent regions either clearly outside the range of WTV (*j*, *l–o*) or unexplored regions (*a–e*, *h–j*, *p*). Sudden breaks in the isobars result from using fast ramps, since the frequency of the inner cylinder rotation is changing significantly within the space–time subset used in the FFT analysis.

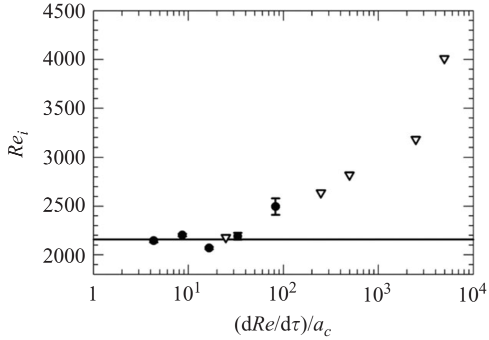

FIGURE 12. Ramp test used to determine the TTV critical condition. Filled circles are the transitions found from the FFT characterization (seen in figure 11). Open triangles are found from tracking the decrease of movement of vortices in the *r–z* plane. The solid line is at $Re = 2160$, ($Re^* = 15.4$), which is the critical condition extrapolated for a ramp of a_c, based on the average of values in the range of $(\mathrm{d}Re/\mathrm{d}\tau)/a_c < 40$.

$2200 < Re_i < 2500$. Similar features are seen in other ramps in figure 11. These could be classified as additional flow states (e.g. MWV_3 and WTV_2) and the onset of TTV could be classified as occurring after the WTV_2 region. For simplicity, we chose not to do so, as the loss of the ω_{WTV} is a sharp, well-defined transition, and the intensity of the post-WTV temporal frequency is relatively weak.

As Re_i is further increased, literature tells us that transitions subsequent to TTV can occur, where another azimuthal wave re-emerges and disappears again (Walden and Donnelly 1979; Takeda 1999; Wang *et al.* 2005) and finally featureless, shear-driven turbulence is observed. Lathrop *et al.* (1992) found this latter transition, where the structure of the turbulence changes to that of simple shear-driven open systems. Using flow visualization, they showed that before the transition, turbulent structures with coherent axial bands (TTV) were found, but after the transition all coherent structure was lost (featureless turbulence). Lewis & Swinney (1999) subsequently determined the same turbulent transition by measuring wave velocity and wall shear stress. For our system, we did not see evidence of a TTV to featureless turbulence transition for Re_i up to at least 3000 ($Re^* = 21.4$); however, access to higher Re^* may yield these additional transitions. The transitions and critical conditions we observed in the present study are included in figures 2 and 8.

4. Conclusions

In this paper, we have focused on higher order transitions in T-C flow with $Re_o = 0$. While a tremendous amount of literature on this problem already exists, we note that the number of parameters is large, resulting in regions of that parameter space that are under-characterized or completely unexplored. For example, $Re_c(\eta, Re_o)$ or even $Re_c(\eta)$ for transitions beyond the primary or secondary instability or quantitative transition characterization for post-chaotic transitions as a function of radius ratio are not available. Ultimately, the knowledge of the Newtonian critical conditions for higher order transitions as a function of geometry is essential for studies of tertiary variables in the T-C geometry. Here, we have summarized results, geometries and protocols from other authors and presented a complete catalogue of new experimental results that address some of the gaps in this parameter space. We used carefully chosen and well-defined ramping protocols, along with flow visualization with a spectral characterization technique that illuminates dynamic transition pathways, and found previously unreported flow states. We found that for our high aspect ratio, narrow gap geometry, the cascade of transitions for Newtonian fluids for $Re_o = 0$ is well described by AZI ⇒ TVF ⇒ WVF ⇔ MWV ⇒ CWV ⇒ WTV ⇒ TTV.

The highly resolved temporal and spatial frequency characterization technique used, similar to that of Takeda (1999) for $Re^* > 7$, has not been previously applied to the early transitions (sub-chaotic flows). Here, it has yielded unique quantification of the dynamics of the frequency cascade through such states as the novel early-modulated waves, the oscillations between single temporal and multiple temporal modes and the onset of chaotic flow states. We found a stabilized early-modulated wavy flow state, where the region of MWV stability was independent of ramp rate (for ramps from $0.26a_c < \mathrm{d}Re/\mathrm{d}\tau < 4.31a_c$). The experiments also showed that the early MWV crosses from the counter- into the co-rotation regime, where the range of stability decreases and a third sub-chaotic WVF emerges with increased Re_o. For $Re_o = 0$, a second WVF (WVF$_2$) is stabilized from $Re^* = 3.56 \pm 0.14$ to $Re^* = 5.20 \pm 0.04$, after which another MWV (MWV$_2$) region forms. The range of stability of MWV$_2$ with no background chaos is significantly smaller than that seen in the literature for smaller radius ratios and lower aspect ratios.

Finally, we presented the characterization of post-chaotic flows as a function of ramp rate. The characterization technique allowed for the tracking of relative mode intensities as a function of Re_i, which leads to an observation of formation and decay of dominant modes. We defined the region of stability of WTV by tracking the onset of a dominant temporal frequency, and the transition to TTV, characterized by the loss of that frequency. While ramp rates of $\mathrm{d}Re/\mathrm{d}\tau > 40a_c$ delay the onset of TTV, it was found that the critical condition for TTV does not change for $\mathrm{d}Re/\mathrm{d}\tau < 40a_c$, likely due to the change in the dominant characteristic length scale. Similar to the situation for MWV$_2$, we see earlier transitions than those reported in the literature for smaller η and $\varGamma$ for CWV at $Re^* = 5.49 \pm 0.05$, WTV at $Re^* \sim 7.85$ and TTV at $Re^* = 15.4$.

Researchers interested in studies of tertiary parameters such as fluid elasticity or cylinder eccentricity on a range of flow types will benefit from the increased library of characterization offered here. Experiments to extend these studies to complex polymeric fluids, for which the present results will serve as important benchmarks, are now underway.

The National Science Foundation has supported this work through Grant CTS-0335169. C. S. Dutcher gratefully acknowledges support from the National Science Foundation Graduate Research Fellowship and the American Association of University Women Engineering Dissertation Year Fellowship.

REFERENCES

Abcha, N., Latrache, N., Dumouchel, F. & Mutabazi, I. 2008 Qualitative relation between reflected light intensity by Kalliroscope flakes and velocity field in the Couette–Taylor flow system. *Exp. Fluids* **45**, 85–94.

Abshagen, J., Lopez, J. M., Marques, F. & Pfister, G. 2005 Mode competition of rotating waves in reflection-symmetric Taylor–Couette flow. *J. Fluid Mech.* **540**, 269–299.

Abshagen, J., Lopez, J. M., Marques, F. & Pfister, G. 2008 Bursting dynamics due to a homoclinic cascade in Taylor–Couette flow. *J. Fluid Mech.* **613**, 357–384.

Abshagen, J., Pfister, G. & Mullin, T. 2001 Gluing bifurcations in a dynamically complicated extended flow. *Phys. Rev. Lett.* **87** (22), 224501.

Abshagen, J., Schulz, A. & Pfister, G. 1996 The Couette–Taylor flow: a paradigmatic system for instabilities, pattern formation and routes to chaos. In *Nonlinear Physics of Complex Systems,* pp. 63–72. Lecture Notes in Physics 476. Springer.

Ahlers, G., Cannell, D. S. & Dominguez-Lerma, M. A. 1983 Possible mechanism for transitions in wavy Taylor-vortex flow. *Phys. Rev.* A **27**, 1225–1227.

Andereck, C. D., Dickman, R. & Swinney, H. L. 1983 New flows in a circular Couette system with co-rotating cylinders. *Phys. Fluids* **26**, 1395–1401.

Andereck, C. D., Liu, S. S. & Swinney, H. L. 1986 Flow regimes in a circular Couette system with independently rotating cylinders. *J. Fluid Mech.* **164**, 155–183.

Avila, M., Marques, F., Lopez, J. M., & Meseguer, A. 2007 Stability control and catastrophic transition in a forced Taylor–Couette system. *J. Fluid Mech.* **590**, 471–496.

Baer, S. M. & Gaekel, E. M. 2008 Slow acceleration and deacceleration through a hopf bifurcation: power ramps, target nucleation, and elliptic bursting. *Phys. Rev.* E **78** (036205).

Barcilon, A., Brindley, J., Lessen, M. & Mobbs, F. R. 1979 Marginal instability in Taylor–Couette flows at a very high Taylor number. *J. Fluid Mech.* **94**, 453–463.

Baxter, G. W. & Andereck, C. D. 1986 Formation of dynamical domains in a circular Couette System. *Phys. Rev. Lett.* **57**, 3046–3049.

Benjamin, T. B. & Mullin, T. 1982 Notes on the multiplicity of flows in the Taylor experiment. *J. Fluid Mech.* **121**, 219–230.

Brandstater, A. & Swinney, H. L. 1987 Strange attractors in weakly turbulent Couette–Taylor flow. *Phys. Rev.* A **35**, 2207–2220.

Cole, J. A. 1976 Taylor-vortex instability and annulus-length effects. *J. Fluid Mech.* **75**, 1–15.

Coles, D. 1965 Transition in circular Couette flow. *J. Fluid Mech.* **21**, 385–425.

Coles, D. 1967 A note on Taylor instability in circular Couette flow. *J. Appl. Mech.* **34**, 529–532.

Coughlin, K. T., Marcus, P. S., Tagg, R. P. & Swinney, H. L. 1991 Distinct quasiperiodic modes with like symmetry in a rotating fluid. *Phys. Rev. Lett.* **66**, 1161–1164.

Czarny, O. & Lueptow, R. M. 2007 Time scales for transition in Taylor–Couette flow. *Phys. Fluids* **19**, 054103.

Czarny, O., Serre, E., Bontoux, P. & Lueptow, R. M 2004 Ekman vortices and the centrifugal instability in counter-rotating cylindrical Couette flow. *Theor. Comput. Fluid Dyn.* **18**, 151–168.

DiPrima, R. C., Eagles, P. M. & Ng, B. S. 1984 The effect of radius ratio on the stability of Couette flow and Taylor vortex flow. *Phys. Fluids* **27**, 2403–2411.

Donnelly, R. J. & Fultz, D. 1960 Experiments on the stability of viscous flow between rotating cylinders. II. Visual observations. *Proc. R. Soc. Lond.* A **258**, 101–122.

Donnelly, R. J. & LaMar, M. M. 1988 Flow and stability of helium II between concentric cylinders. *J. Fluid Mech.* **186**, 163–198.

Donnelly, R. J., Park, K., Shaw, R. & Walden, R. W. 1980 Early nonperiodic transitions in Couette flow. *Phys. Rev. Lett.* **44**, 987–989.

Dutcher, C. S. & Muller, S. J. 2007 Explicit analytic formulas for Newtonian Taylor–Couette primary instabilities. *Phys. Rev.* E **75**, 047301.

Esser, A. & Grossmann, S. 1996 Analytic expression for Taylor–Couette stability boundary. *Phys. Fluids.* **8**, 1814–1819.

Fenstermacher, P. R., Swinney, H. L. & Gollub, J. P. 1979 Dynamical instabilities and the transition to chaotic Taylor vortex flow. *J. Fluid Mech.* **94**, 103–128.

Gollub, J. P. & Swinney, H. L. 1975 Onset of turbulence in a rotating fluid. *Phys. Rev. Lett.* **35**, 927–930.

Gorman, M. & Swinney, H. L. 1982 Spatial and temporal characteristics of modulated waves in the circular Couette system. *J. Fluid Mech.* **117**, 123–142.

Hegseth, J. J., Baxter, G. W. & Andereck, C. D. 1996 Bifurcations from Taylor vortices between corotating concentric cylinders. *Phys. Rev.* E **53**, 507–521.

King, G. P. & Swinney, H. L. 1983 Limits of stability and irregular flow patterns in wavy vortex flow. *Phys. Rev.* A **27**, 1240–1243.

Koschmieder, E. L. 1979 Turbulent Taylor vortex flow. *J. Fluid Mech.* **93**, 515–527.

Koschmieder, E. L. 1993 *Bénard Cells and Taylor Vortices.* Cambridge University Press.

Lathrop, D. P., Fineberg, J. & Swinney, H. L. 1992 Transition to shear-driven turbulence in Couette–Taylor flow. *Phys. Rev.* A **46**, 6390–6405.

LEWIS, G. S. & SWINNEY, H. L. 1999 Velocity structure functions, scaling, and transitions in high-Reynolds-number Couette–Taylor flow. *Phys. Rev.* E **59**, 5457–5467.

MEINCKE, O. & EGBERS, C. 1999 Route into chaos in small and wide gap Taylor–Couette flow. *Phys. Chem. Earth* B **25**, 467–471.

MULLIN, T. 1985 Onset of time dependence in Taylor–Couette flow. *Phys. Rev.* A **31**, 1216–1218.

PARK, K. & CRAWFORD, G. L. 1983 Deterministic transition in Taylor wavy-vortex flow. *Phys. Rev. Lett.* **50**, 343–346.

PARK, K., CRAWFORD, G. L. & DONNELLY, R. J. 1981 Determination of transition in Couette flow in finite geometries. *Phys. Rev. Lett.* **47**, 1448–1450.

PFISTER, G. & GERDTS, U. 1981 Dynamics of Taylor wavy vortex flow. *Phys. Lett.* **83A** (1), 23–25.

SINHA, M., KEVREKIDIS, I. G. & SMITS, A. J. 2006 Experimental study of a Neimark–Sacker bifurcation in axially forced Taylor–Couette flow. *J. Fluid Mech.* **558**, 1–32.

SMITH, G. P. & TOWNSEND, A. A. 1982 Turbulent Couette flow between concentric cylinders at large Taylor numbers. *J. Fluid Mech.* **123**, 187–217.

SNYDER, H. A. 1968 Stability of rotating Couette flow. II. Comparison with numerical results. *Phys. Fluids* **11**, 1599–1605.

SNYDER, H. A. 1969 Wave-number selection at finite amplitude in rotating Couette flow. *J. Fluid Mech.* **35**, 273–298.

TAGG, R. 1994 The Couette–Taylor problem. *Nonlinear Sci. Today* **4**, 2–25.

TAKEDA, Y. 1999 Quasi-periodic state and transition to turbulence in a rotating Couette system. *J. Fluid Mech.* **389**, 81–99.

TAKEDA, Y., FISCHER, W. E., KOBASHI, K. & TAKEDA, T. 1992 Spatial characteristics of dynamic properties of modulated wavy vortex flow in a rotating Couette system. *Exp. Fluids* **13**, 199–207.

TAKEDA, Y., FISCHER, W. E., SAKAKIBARA, J. & OHMURA, K. 1993 Experimental observation of the quasiperiodic modes in a rotating Couette system. *Phys. Rev.* E **47**, 4130–4134.

TAYLOR, G. I. 1923 Flow regimes in a circular Couette system with independently rotating cylinders. *Phil. Trans. R. Soc. Lond.* A **223**, 289–343.

VON STAMM, J., GERDTS, U., BUZUG, TH. & PFISTER, G. 1996 Symmetry breaking and period doubling on a torus in the VLF regime in Taylor–Couette flow. *Phys. Rev.* E **54**, 4938–4957.

WALDEN, R. W. & DONNELLY, R. J. 1979 Reemergent order of chaotic circular Couette flow. *Phys. Rev. Lett* **42**, 301–304.

WANG, L., OLSEN, M. G. & VIGIL, R. D. 2005 Reappearance of azimuthal waves in turbulent Taylor–Couette flow at large aspect ratio. *Chem. Engng Sci.* **60**, 5555–5568.

WHITE, J. 2002 Experimental investigation of instabilities in Newtonian and viscoelastic Taylor–Couette flows. PhD dissertation, University of California, Berkeley.

XIAO, Q., LIM, T. T. & CHEW, Y. T. 2002 Effect of acceleration on the wavy Taylor vortex flow. *Exp. Fluids* **32**, 639–644.

ZHANG, L. H. & SWINNEY, H. L. 1985 Nonpropagating oscillatory modes in Couette–Taylor flow. *Phys. Rev.* A **31**, 1006–1009.